CRYSTAL GROWTH & DESIGN

Article

pubs.acs.org/crystal

Competitive Growth of Scrutinyite (α-PbO_2) and Rutile Polymorphs of SnO_2 on All Orientations of Columbite $CoNb_2O_6$ Substrates

Julia Wittkamper,[†] Zhongnan Xu,[‡] Boopathy Kombaiah,[†,§] Farangis Ram,[†] Marc De Graef,[†] John R. Kitchin,[‡] Gregory S. Rohrer,[†] and Paul A. Salvador*,[†]

[†]Department of Materials Science and Engineering and [‡]Department of Chemical Engineering, Carnegie Mellon University, 5000 Forbes Avenue, Pittsburgh, Pennsylvania 15213, United States

Supporting Information

ABSTRACT: Combinatorial substrate epitaxy (CSE) is used to investigate polymorph competition between metastable scrutinyite (α-PbO_2) structured (*s*-) and stable rutile structured (*r*-) SnO_2 during local epitaxial growth across orientation space on polycrystalline columbite (*c*-) $CoNb_2O_6$ substrates. Growth occurs in a grain-over-grain fashion, where individual grains of *c*-$CoNb_2O_6$ support the growth of individual grains of SnO_2. Both metastable *s*-SnO_2 and stable *r*-SnO_2 crystals are observed, each growing on specific ranges of substrate orientations and each having a single specific orientation relationship (OR) with substrate grains on which it grew. *s*-SnO_2 adopts the unit-cell over unit-cell OR that can be expressed as the alignment of primary eutactic planes: $(100)_{s*}[001]_{s*}\|(100)_{c*}[001]_{c*}$ (where the * indicates the use of Pcnb setting). *s*-SnO_2 grains grow on a slight majority of orientations and specifically on orientations inclined from the (010) pole of *c**-$CoNb_2O_6$. *r*-SnO_2 adopts an OR that can be expressed as the alignment of a secondary set of eutactic planes: $(101)_r[010]_r\|(010)_{c*}[001]_{c*}$. *r*-$SnO_2$ grows only on orientations close to the (010) pole of *c**-$CoNb_2O_6$. The collected set of observations is discussed and rationalized with respect to the combination of misfit strain energies and cation packing interfacial energy penalties. We conclude that CSE should allow for the rational and computationally guided development of new materials adopting scrutinyite, rutile, and related structures.

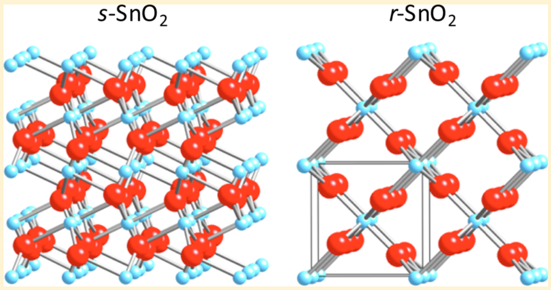

1. INTRODUCTION

Directed synthesis methods that access specific crystalline polymorphs are of great interest in crystal growth and materials design because polymorphs of identical compositions often exhibit remarkably different properties.[1−5] The experimentally observed polymorph is a function of temperature, pressure, particle size, and reaction pathway.[1−4,6−8] Most polymorph-specific synthesis methods have been found by trial and error (along with chemical intuition).[4] Recently, computational models of polymorph stability have found success in matching transformation conditions as a function of pressure[7,9−13] or versus particles size.[14−19] Such results are encouraging for the development of computationally guided synthesis. However, not all polymorphs can be stabilized by pressure or particle size; thus, other directed synthesis methods are needed.

Epitaxial stabilization is the directed growth of a specific polymorph for a film (of a given composition) owing to the interaction between the nucleating film and supporting substrate.[20−24] It has been used extensively for the synthesis of metastable polymorphs, including some which have not been observed using other synthesis methods.[20−28] Recent work indicates that computational guidance to epitaxial stabilization could be as effective as it has been for pressure and size effects.[29−33] Ultimately, epitaxial stabilization is constrained by (1) the relative energetic differences between polymorphs, which are often unknown; and (2) the abilities of available substrates to direct polymorph specific growth, which are often determined in a trial-by-error fashion using a limited set of commercially available substrates. Herein, we address the constraints to epitaxial stabilization of scrutinyite (the mineral name of α-PbO_2) polymorphs,[30] describing the competitive growth of rutile (*r*-) and scrutinyite (*s*-) SnO_2 on polycrystalline columbite (*c*-) substrates ($CoNb_2O_6$), for surfaces across all of orientation space.

Tin dioxide, SnO_2, has many uses, including as a transparent conductor, catalyst, and gas sensor.[8,34−36] SnO_2 adopts a rutile structure for the most stable polymorph at ambient pressures, but other polymorphs, including a scrutinyite-structured one, are known to form at high pressures,[8,12,13,37,38] in nanostructures,[39,40] or as thin films.[41−44] When compared to the *r*-SnO_2 phase, *s*-SnO_2 has a decreased electrical resistivity,[44,45] an increased sensitivity to CO,[45] and applications in capacitors when combined with other phases.[40] From a stability point of view, *s*-SnO_2 is ~6 kJ/mol less stable than *r*-SnO_2,[30] indicating it is a prime candidate to explore using epitaxial stabilization. In fact, *s*-SnO_2 has been stabilized as epitaxial thin films on yttrium-stabilized zirconia (YSZ) single crystals.[42,43,45,46] The orientation and phase of those SnO_2 films are strong functions of

Received: April 20, 2017
Revised: June 1, 2017
Published: June 5, 2017

DOI: 10.1021/acs.cgd.7b00569
Cryst. Growth Des. 2017, 17, 3929−3939

temperature and orientation of the fluorite substrate, which is not structurally well-matched to either polymorph.

Crystals that are isostructural to the target polymorph, with similar lattice parameters, are the preferred substrates for epitaxial stabilization, but these are not commercially available for scrutinyite structured materials. This absence limits the range of metastability that can be surmounted in epitaxial stabilization, especially for similarly structured polymorphs like rutile and scrutinyite. For example, *r*-RuO_2 is ∼13 kJ/mol[30] more stable than *s*-RuO_2, and the latter has never been observed.[47] Xu and Kitchin[48] compared the computational activity of scrutinyite (therien called columbite) and rutile dioxides (BO_2, B = Ru, Rh, Pt, Ir) and asserted that the scrutinyite IrO_2 polymorph should have one of the lowest overpotentials for the oxygen evolution reaction amongst known materials. *s*-IrO_2 is >20 kJ/mol less stable than *r*-IrO_2[30] and has never been observed. While we have approximated 20 kJ/mol[30] as a ballpark value that can be overcome in epitaxy, this number involves several approximations for the energetic terms associated with interactions between specific film−substrate pairs. The question of interest therefore is what substrate would be the most robust for the stabilization of scrutinyite polymorphs? Using SnO_2 as a prime example of phase competition between rutile and scrutinyite polymorphs, since it is known to exist and has only a 6 kJ/mol energetic difference, we explore this question herein.

A brief consideration of the structures of the relevant polymorphs (details are given in the Supporting Information (SI), §S1−S3) is necessary to understand the challenge of identifying a robust polymorph differentiating substrate. Rutile and scrutinyite are often described as having hexagonally stacked (100) planes of nearly close packed oxide ions (i.e., eutactic stacking,[49] even though the planes are heavily distorted).[50] Thus, from the anion packing perspective, there is little differentiation between these structures, and anion packing will not impact substrate choice (unlike for the rutile and cubic close packed anatase phase competition on ABO_3 compounds[29]). In rutile and scrutinyite, the cations occupy 1/2 of the octahedral interstices in the eutactic network. In between the $(100)_r$ eutactic planes of rutile, the cations occupy fully every other $[01\bar{1}]_r$ row (see Figure S1a; we call this the $c_{1/2\text{-}I}$ pattern). In between the $(100)_{s*}$ eutactic planes of scrutinyite* (the notation * denotes the use of the *Pcnb* setting) the cations alternate occupation in every row, resulting in zigzag patterns running along the $[010]_{s*}$ (see Figure S2a; we call this the $c_{1/2\text{-}II}$ pattern). Stacking the $(100)_r$ eutactic plane epitaxially on the $(100)_{s*}$ eutactic plane of a substrate, a potential low-energy epitaxial orientation relationship (OR), will result in energetic penalties from disturbances in the cation packing at the interface. Thus, a substrate that can differentiate between scrutinyite and rutile during epitaxial nucleation, and continued growth, must differ in the interfacial energies from either different cation ordering or the volumetric strain energies in coherent growth. To minimize the first penalty for scrutinyite, cation packing in the ideal substrate should be similar to that in scrutinyite and dissimilar to that in rutile (as much as that is possible). Epitaxial misfit strains (see §S5) are related to the epitaxial OR and the lattice parameters, and these should be minimized in the ideal substrate to stabilize scrutinyite. More detailed descriptions of crystallography, cation packing, eutactic planes, potential epitaxial ORs, and epitaxial cationic packing disturbances and epitaxial strains are given in the SI (§S1−5).

Columbite (*c*-) is a derivative of the scrutinyite structure that forms readily for many compounds of stoichiometry $B'B_2O_6$,[51−53] where the B' cation is ordered into every third $(100)_{s*}$ plane in the scrutinyite structure. Several phases, including *c**-$CoNb_2O_6$ (*c**- indicates columbite in a *Pcnb* setting) have reasonably similar lattice parameters to those of *s**-SnO_2.[54,55] Though single crystals are not available, *c*-$CoNb_2O_6$ can be readily made as large grained dense polycrystals, appropriate for use as substrates in the high-throughput epitaxial synthesis approach we call combinatorial substrate epitaxy (CSE).[25,56−61] In CSE, locally epitaxial films are deposited on the surfaces of large-grained polished polycrystals and are characterized for their local growth using electron backscatter diffraction (EBSD) in a scanning electron microscope (SEM). While columbite structured substrates seem like ideal substrates for growth of *s*-SnO_2 (and other scrutinyite structured materials), we still do not know the answers to two basic questions. (1) How do *r*-SnO_2 and *s*-SnO_2 grow epitaxially upon columbite? (2) Is *r*-SnO_2 sufficiently destabilized to allow for *s*-SnO_2 growth on columbite? The purpose of this article is to answer these questions for *c*-$CoNb_2O_6$ surfaces across all orientation space and to shed light on the energetic nature of the cation packing penalties and epitaxial strains for each polymorph. This work contributes to directed synthesis of materials by epitaxy.

2. EXPERIMENTAL SECTION

c-$CoNb_2O_6$ was made using stoichiometric amounts of Nb_2O_5 (AlfaAesar, 99.9%) and Co_3O_4 (Aldrich, 99.5%). The powders were combined in ethanol, ball milled (with YSZ grinding media) wet for ∼12 h, dried, and uniaxially pressed (in a stainless steel die) into pellets of ∼1 cm diameter and between 1 and 2 mm in thickness. The pellets were reacted at 900 °C for 8 h in air, cooled, reground, and ball milled dry for ∼24 h. The powders were uniaxially pressed (with a few drops of polyvinyl alcohol as a binder) into pellets of 1 cm. The pellets were annealed in a three stage process, with heating and cooling rates of ∼10 °C/min: 1 h at 750 °C (to ensure all binder was removed), 3 h at 1150 °C (to sinter the pellets), and 40 h at 1240 °C (to allow for grain growth). The grain sizes ranged from 5 to 70 μm, which are appropriate for EBSD characterization used in CSE. Sintered substrates were polished to a mirror finish, with sequential steps from 180 grit SiC to 0.01 μm Al_2O_3, and annealed for 2 h at 800 °C (to heal polishing damage; little thermal grooving or roughening was observed). It should be noted that grain pullout during polishing was common and that the surfaces had a significant number of missing grains, which may impact the thermal distribution at the surface. Prior to growth, substrates were ultrasonically cleaned in methanol and then acetone, dried with compressed air, and attached to the substrate heater with silver paint.

SnO_2 films were fabricated by pulsed laser deposition, using a system applied extensively for CSE growth.[25,56−58] A KrF laser (λ = 248 nm) was pulsed between 1 and 3 Hz and focused to areal laser energy densities between 0.5 to 2 J/cm^2. Films were deposited at 700 °C in an oxygen pressure of ∼50 mTorr with a target to substrate distance of ∼6 cm. The growth rate, measured using X-ray reflectivity (of films grown on commercial single crystals), ranged from 0.03 Å/pulse (called the low growth rate, or lgr) to 0.6 Å/pulse (called the high growth rate, or hgr).

Substrates and films were characterized for their local structure using EBSD in an SEM.[25,56−58] Experiments were carried out using a Quanta 200 SEM (FEI Company) with an accelerating voltage of 15.0 kV, a spot size of 4−5, a working distance of 11.6 mm, and a tilt angle of 70° from horizontal. Experiments were done in a high vacuum ($\sim 3.36 \times 10^{-6}$ Torr). To avoid charging, graphite paint was applied along the edges of the sample to create a connection to the back contact of the mount. Other parameters, such as contrast and brightness, were adjusted manually during each experiment to yield quality patterns.

Background subtracted patterns were automatically indexed using the TSL software, and the structural information is given in the SI for *c**-$CoNb_2O_6$ and *s**-SnO_2 in the nonstandard *Pcnb* settings, and *r*-SnO_2 in the standard $P4_2/mnm$ setting. The data was processed with one iteration of a grain dilation algorithm (with a minimum grain size of 5 pixels and a grain tolerance angle of 5°) and subsequently by assigning a single average orientation to each grain (averaging the orientation of all points within the identified grain). The ORs between film/substrate pairs were determined using methods described elsewhere.[57] Because the structures of *s*-SnO_2 and *r*-SnO_2 are so similar, and some grains could be indexed in both systems, we also indexed the EBSD patterns of select areas using in-house programs that compare experimental and simulated EBSD patterns directly. Simulations and indexing were done in a fashion similar to that reported elsewhere,[62−64] and using parameters given in the SI (§S8).

Transmission electron microscopy (TEM) was carried out on select grains to confirm the successful fabrication of *s*-SnO_2. TEM samples were prepared using a focused ion beam (FIB) lift-out approach in a Nova 600 (FEI, Oregon) dual-beam SEM. Samples were prepared on specific grains to expose specific zone axes identified with EBSD in the same Nova 600 SEM (see SI, Figure S10). The preparation method is described elsewhere.[25] Selected-area electron diffraction (SAED) patterns and bright field images were recorded using an FEI Tecnai F20 field emission gun microscope operated at 200 kV, whereas the corresponding high-resolution (HR) TEM images were recorded using an image-aberration corrected 300 kV FEI TITAN G2 80−300 microscope.

3. RESULTS

3A. Grain-over-Grain Growth. Figure 1a,b gives inverse pole figure (*IPF*) maps (at 0.12 *μ*m resolution) of (a) a *c**-$CoNb_2O_6$ substrate and (b) the lgr SnO_2 film (∼20 nm thick) grown upon the same region. Note there is a slight rotation and change in aspect ratio between (a) and (b), so the regions do not overlap perfectly. In Figure 1b, the film grains were indexed using both *s**-SnO_2 and *r*-SnO_2 structures, and the phase of each grain is noted.

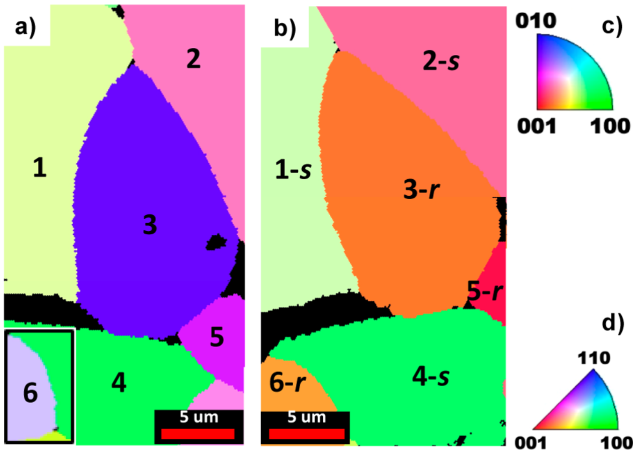

Figure 1. Processed IPF maps (with a pixel spacing of 0.12 *μ*m) from (a) the substrate, indexed as *c**-$CoNb_2O_6$, and (b) the overlaying film, indexed as the best match for both *s**-SnO_2 and *r*-SnO_2. The color keys are given in (c) for *c**-$CoNb_2O_6$ and *s**-SnO_2 and in (d) for *r*-SnO_2. The area and aspect ratio of (a) is slightly different from (b), and the region of grain 6 in (a) is an inset. Six grains common to both are marked in (a) and (b), with the phase of each film grain also marked in (b).

The results in Figure 1 demonstrate that growth proceeds in a grain-over-grain fashion. Each grain in the substrate has a single overlaying grain in the film, with the same shape and boundaries. This is readily observed for grain 3 and by the locations of boundaries between all grains. This is not an artifact of processing; most points in the IPF map were well indexed, as indicated by the unprocessed IPF maps shown in Figure S5. In general, the EBSD patterns were strong for both the substrate and film, with the former being sharper and more intense. Processing the raw data simply removes poorly indexed points, which are a small fraction of the overall data. Image quality (IQ) maps from this region are shown in Figure S6, where one can see grain boundaries and residual scratches. Dark regions in the IQ maps correlate with the poorly indexed regions in the IPF maps. These observations indicate that the processed IPF maps are a strong indicator of local epitaxial growth and can be used to further characterize growth across orientation space.

3B. Positive Phase Identification. The results in Figure 1 also demonstrate that both *s*-SnO_2 and *r*-SnO_2 are observed in the film. In Figure 1, grains 1, 2, and 4 (3, 5, and 6) were indexed best in the *s*-SnO_2 (*r*-SnO_2) structure. As described previously, the scrutinyite and rutile structures are quite similar. Nevertheless, the commercial software consistently indexed some grains better as one phase than the other (see also IPF maps in Figures 2,3, and S8). The commercial software uses a Hough transformation of the diffraction pattern and a ranking method based on user-supplied data about expected diffraction bands. To ensure that the EBSD processing could indeed differentiate between these two derivatives of hexagonally packed eutactic structures, we used an independent in-house indexing method that involves EBSD simulations and whole-pattern comparisons

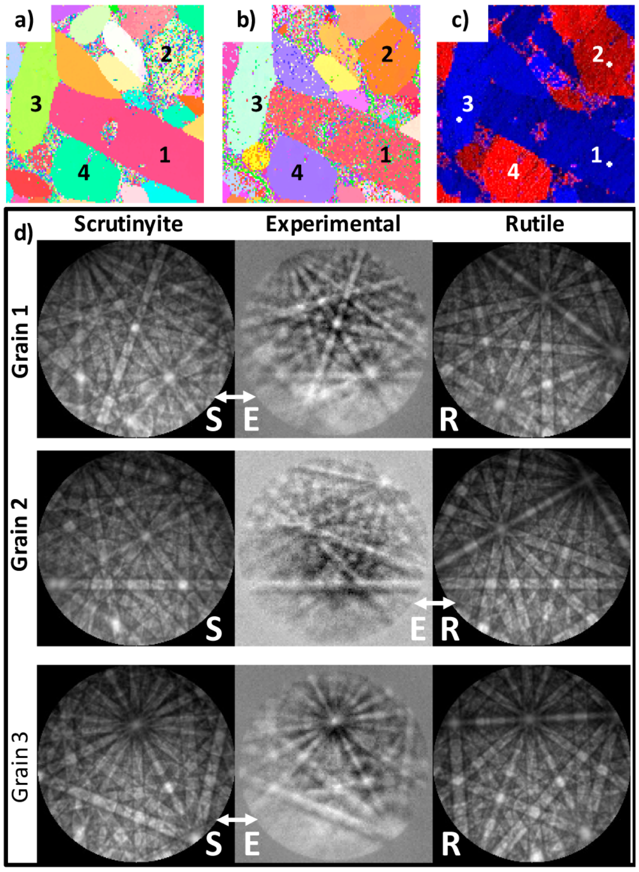

Figure 2. IPF maps (with a pixel spacing of 0.4 *μ*m) indexed using in-house methods in (a) *s**-SnO_2 and (b) *r*-SnO_2 structures. The horizontal (vertical) distance is 52.8 (58) *μ*m, and the color keys are given in Figure 1c,d. The better matched phase is given in (c), with blue (red) indicating *s*-SnO_2 (*r*-SnO_2). (d) The experimental pattern (central column) and best matched simulated pattern for *s**-SnO_2 (left column) and *r*-SnO_2 (right column), for grains 1, 2, and 3 (top, middle, and bottom row, respectively).

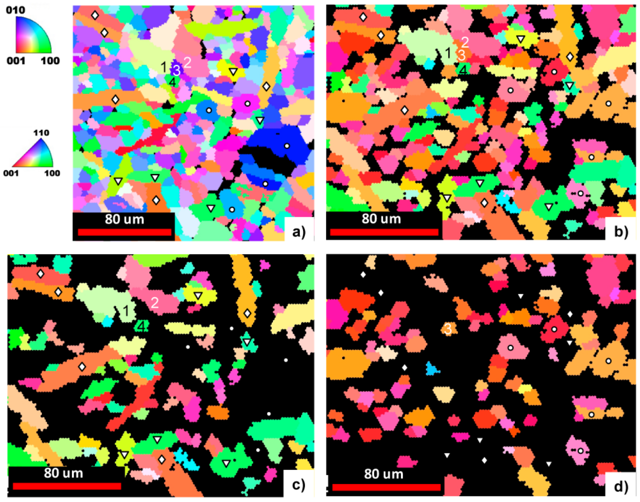

Figure 3. Large area IPF (pixel size 1.5 μm) maps from (a) the substrate c^*-$CoNb_2O_6$ and (b) the overlaying film, indexed as the best match for both s^*-SnO_2 and r-SnO_2. The same information as (b) is shown (c) and (d), with s^*-SnO_2 orientations in (c) and r-SnO_2 orientations in (d). Color keys are shown to the left of panel (a) for c^*-$CoNb_2O_6$ and s^*-SnO_2 (upper) and rutile (lower). The area and aspect ratio of (a) is slightly different from the others. Some locations in each are marked with different symbols or numbers, as described in the text.

of experimental patterns to simulated patterns of all potential orientations.[62−64] High-resolution small area unprocessed IPF maps of the lgr SnO_2 film are given in Figure 2, generated using the in-house method on a different area of the film. In Figure 2, the film was indexed as (a) s^*-SnO_2 and (b) r-SnO_2 structures. The best fit phase for each EBSD pattern is shown in Figure 2c, where blue (red) indicates s-SnO_2 (r-SnO_2). The shape of the film grains are consistent with grain-over-grain growth, with a single orientation per grain, and with some grains being s-SnO_2 and some being r-SnO_2.

For most grains in Figure 2a,b, patterns could be indexed as either phase. For some grains, e.g., 1 and 2, one can comment on the quality of the indexing by the number of poorly indexed points. For other grains, e.g., 3 and 4, the entire grains are well indexed in both phases. The experimental patterns from grains 1, 2, and 3 are given in Figure 2d as the central column of the lower panel. These can be compared to the simulated patterns of the best fit orientations of the s-SnO_2 (r-SnO_2) phase, given in the left (right) column of the lower panel of Figure 2d. Visual inspection of the patterns from grains 1 and 2 allows one to make a relatively easy assignment to the better fit, which agrees with the observations that the patterns are similar, but differentiable. However, differentiation by visual inspection is more difficult for grain 3, but differences are observable. This is reinforced by the results of the whole pattern comparison algorithms, which consistently lead to a better fit for s-SnO_2. This supports the idea that the two phases are clearly differentiable using EBSD alone, and supports the fabrication of s-SnO_2 on entire, but specific, grains of c-$CoNb_2O_6$.

3C. Epitaxial Orientation Relationships (ORS). To determine the preferred epitaxial OR for both phases, many more observations are needed than those given in Figures 1 and 2. Figure 3a,b gives large area IPF maps (pixel size 1.5 μm) of (a) a c^*-$CoNb_2O_6$ substrate and (b) the lgr SnO_2 film grown upon it. In Figure 3b, film grains were indexed using both s^*-SnO_2 and r-SnO_2 structures. (The unprocessed IPF maps at this resolution are shown in Figure S7.) These images are representative of all large-area IPF maps observed. (A similarly processed IPF map from the hgr film is given in Figure S8.) For the substrate, the grain sizes and shapes vary, with characteristic lengths on the order of several ones to several tens of microns and shapes from equiaxed to acicular. In all IPF maps, black pixels indicate unindexed pixels; these generally correspond to empty space left by pores or grain pullout. Grains 1−4 in Figure 3 are the same as those in Figure 1. Fifteen other locations are marked in Figure 3 with symbols to assist in locating similar regions and in describing the results. These IPF maps reinforce the grain-over-grain and mixed phase growth observed in Figures 1 and 2.

In Figures 1 and 2, the colors of s^*-SnO_2 grains appear to be the same as the c^*-$CoNb_2O_6$ grains on which they grew, consistent with the expected unit-cell over unit-cell epitaxial OR. However, the colors of the r-SnO_2 grains differ from those of the underlying c^*-$CoNb_2O_6$ grains. Figure 3 further emphasizes that the film has more than one OR between the film and substrate. While the substrate IPF map has no preferential orientation, the film IPF map has a clear preference for near (001) orientations indicated by red/orange colored grains, with some (100) (green) grains also appearing. Figure 3c,d presents the film *IPF* maps broken into (c) the s^*-SnO_2 grains and (d) the r-SnO_2 grains. The s^*-SnO_2 grains are colored red to green, while r-SnO_2 grains are red-toned. The preference for specific orientations in the film may come from multiple ORs across orientation space or preferred growth in different regions of orientation space. We address the first cause here.

A total of 135 substrate−film grain pairs were identified from various regions of the film, selected to be spread across substrate orientation space, with 66 (69) film grains indexed as s^*-SnO_2 (r-SnO_2). The epitaxial ORs were determined using in-house programs that determine the angles between crystallographic vectors in the films and substrates based on the orientations determined from EBSD. For eutactic structures such as rutile, scrutinyite, and columbite, we expect one low-energy OR to be the alignment of the eutactic networks between the structures.[58] As described previously, there are several types of nearly eutactic planes in these structures, so there are possibly degenerate ORs, even for eutaxial growth (epitaxial growth exhibiting a eutactic OR).

In Figure 4a, we plot the angles between the normal to the primary (100) eutactic planes (out-of-plane), for 66 s^*-SnO_2 grains, and the inset is the angle between similar [001] directions in the eutactic planes (in-plane). Sixty-five of 66 grains are aligned similarly with the substrate (we did not further investigate the outlier). We call this epitaxial OR the primary eutaxial OR: $(100)_{s^*}[001]_{s^*}\|(100)_{c^*}[001]_{c^*}$. This is equivalent to a unit-cell over unit-cell epitaxial OR. The 65 s^*-SnO_2 grains have an average misorientation of 5.6° and 6.2° for the out-of-plane and in-plane directions, respectively. In Figure 4b, we plot the angles between the normal to a secondary set (see §S1−S3) of eutactic planes (out-of-plane), for the 69 r-SnO_2 grains, and the inset is the angle between similar directions in the secondary eutactic planes (in-plane). Sixty-four of 69 r-SnO_2 grains are aligned similarly with the substrate (we did not further investigate the outliers), adopting a secondary eutaxial OR: $\{101\}_r\langle 010\rangle_r\|(010)_{c^*}[001]_{c^*}$. The 64 r-SnO_2 grains have an average misorientation of 7.5° and 7.5° for the out-of-plane and in-plane directions, respectively. The spread in angular orientation is likely due to specific relaxations of interfacial mismatches for different orientations. These observations indicate that each phase adopts a single OR, regardless of its orientation; the observed ORs are eutaxial ORs, and the film

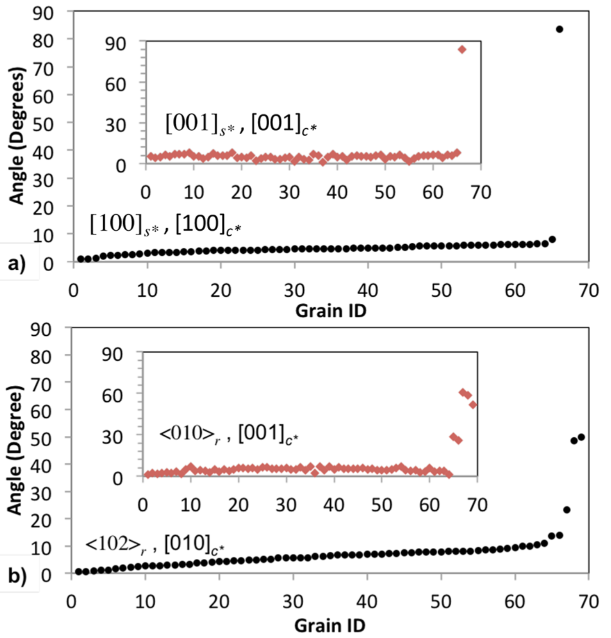

Figure 4. Angle between: (a) the normals to the $(100)_{s*/c*}$ primary eutactic planes, i.e., $[100]_{s*/c*}$, and (inset) the in-plane $[001]_{s*/c*}$ directions for the s*-SnO$_2$ grains and c*-CoNb$_2$O$_6$ substrates; (b) the normals to the secondary eutactic planes $\{101\}_r$ and $(010)_{c*}$, i.e., $\sim\langle 102\rangle_r$ and $[010]_{c*}$, and (inset) the in-plane $\langle 010\rangle_r$ and $[001]_{c*}$ directions for the r-SnO$_2$ grains and c*-CoNb$_2$O$_6$ substrates.

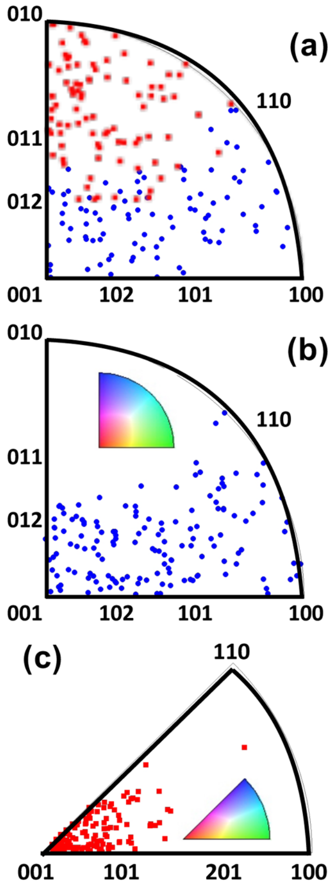

Figure 5. Orientations of 135 grain pairs that were used to determine the epitaxial ORs, plotted using standard stereographic projections of the domain of unique orientations. Blue circles (red squares) indicate s*-SnO$_2$ (r-SnO$_2$) film grains. The location of points indicates the orientation of (a) the c*-CoNb$_2$O$_6$ substrate grain on which the phase grew, (b) s*-SnO$_2$ grains, and (c) r-SnO$_2$ grains.

aligns one of its eutactic planes with one of the substrate's; while orientation does not impact the epitaxial OR of either phase, it influences local relaxation mechanisms.

3D. Orientation-Dependent Phase Selection.

The data in Figures 1−3 indicate that certain orientations stabilize epitaxial s-SnO$_2$ grains, while other orientations support epitaxial r-SnO$_2$ growth. The s*-SnO$_2$ film grains lack $(010)_{s*}$ orientations (blue). Instead, there is a preponderance of $(001)_{s*}$ and $(100)_{s*}$ poles (green to red). For the r-SnO$_2$ grains, the orientations indicate a clear preference for (001) (red and orange). In Figure 3, five grains that have substrate orientations in the red to orange, green to yellow, and magenta to blue color ranges are denoted, respectively, with diamonds, triangles, and circles. For the diamond and triangle (circle) grains, the film grains index as s*-SnO$_2$ (r-SnO$_2$).

For the 135 grains whose ORs were presented in Figure 4, the phase that each grain adopted is plotted versus the orientation of the underlying substrate grain on a stereographic projection in Figure 5a. These results clearly demonstrate that c*-CoNb$_2$O$_6$ grains between $(001)_{c*}$ and $(100)_{c*}$ support s-SnO$_2$ growth, while grains near $(010)_{c*}$ support r-SnO$_2$ growth. Slightly more of orientation space favors s-SnO$_2$ growth than r-SnO$_2$. The line of demarcation is approximately connecting the $(012)_{c*}$ and $(110)_{c*}$ orientations. Only near the demarcation line are both phases observed for similar substrate orientations.[57]

The orientation of the s*-SnO$_2$ grains are shown in Figure 5b, and they exhibit nearly an identical distribution to the substrate grains on which they grew. The diamond and triangle grains in Figure 3 (and grains 1, 2, and 4 in Figure 1) are examples of such grains having the primary eutaxial OR. The orientation of the r-SnO$_2$ grains are shown in Figure 5c, and these are clustered near the r-(001) orientation, indicating a significant orientation change from the substrate grains on which they grew. The circle grains in Figure 3 (and grains 3, 5, and 6 in Figure 1) are examples of such grains having the secondary eutaxial OR. The color legends for both orientation spaces are given as insets. The substrate and film grain orientations in Figures 1 and 3 can be understood based on the orientation-dependent phase selectivity in combination with the specific primary epitaxial OR observed for each phase.

Figure S8 shows a similar comparison of large area low-resolution IPF maps for the hgr film, and Figure S9 shows the epitaxial ORs for select film/substrate grain pairs from the hgr film. Those results are consistent with the results from the lgr film: grain-over-grain growth of a two-phase film, with c*-CoNb$_2$O$_6$ orientations between (001) and (100) stabilizing s*-SnO$_2$ grains with the primary eutaxial OR and with c*-CoNb$_2$O$_6$ orientations near (010) stabilizing r-SnO$_2$ grains with the secondary eutaxial OR. These four observations were not strong functions of growth rate, but the quality of the EBSD patterns and overall number of grains that were well indexed were consistent with local epitaxial growth being frustrated at higher growth rates. Moreover, there were consistently fewer s-SnO$_2$ grains in the hgr films and more of the s-SnO$_2$ had (100) orientations, suggesting that this orientation of c*-CoNb$_2$O$_6$ is the most robust for stabilizing s-SnO$_2$. Thus, the growth rate appears to impact the relative area and line of demarcation of phase stability in orientation space (Figure 5), but we did not investigate this further.

DOI: 10.1021/acs.cgd.7b00569
Cryst. Growth Des. 2017, 17, 3929−3939

3E. Transmission Electron Microscopy. To corroborate the EBSD characterization of s-SnO_2 growth, we prepared TEM specimens of film grains having nearly $(100)_{c/s}$ surface planes for both the lgr and hgr films. IPF maps of the samples taken prior to FIB specimen preparation are shown in Figure S10, with the specific specimen grains indicated. The in-plane orientation data was used to orient the sample near a (001) zone axis for FIB sample preparation. Unfortunately, the sample milling process damaged the outer portions of the films, on the order of 10−15 nm near the film surface. For the 20 nm lgr film, this lead to only a small portion of the film/substrate interfacial region remaining at the surface (see Figure S11). For the 100 nm hgr film, only the topmost portion of the surface was damaged, and the vast majority of the film was unaffected (see Figure 6). We focus on the hgr film here because it demonstrates both the successful growth of s-SnO_2 and the robustness of growth through the thickness of the film even at high growth rates. Similar lgr results are given in Figure S11.

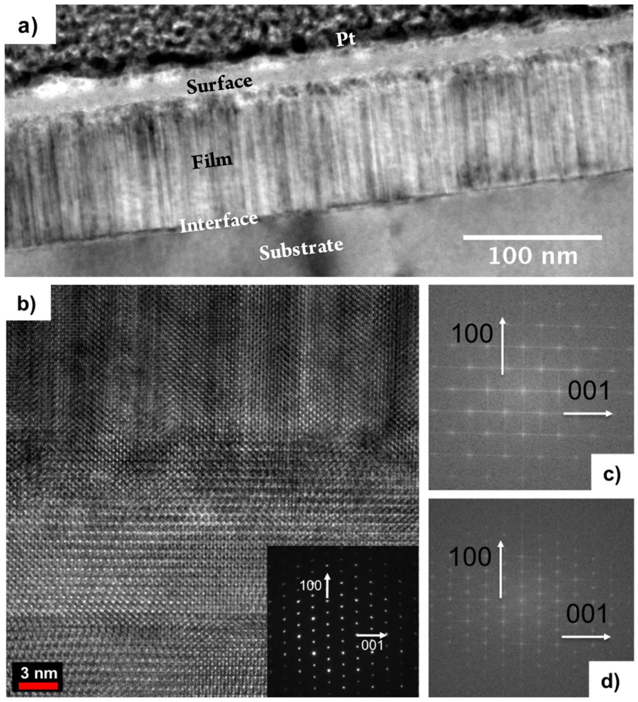

Figure 6. (a) Low-resolution TEM image of the hgr 100 nm thick film. (b) A high-resolution TEM image of the interfacial region: the substrate is on the bottom and columnar grain on the top, with the interface between them. The inset shows the SAED image, indicating the (001) zone with only one apparent set of spots observable. Fast Fourier transforms of (c) the film and (d) the substrate support the phase assignments.

A low-resolution bright field TEM image of the hgr film−substrate interface region is shown in Figure 6a. The substrate, substrate−film interface, film, damaged surface region, and Pt overlayer are marked. The damaged surface region is quite extensive and may either be connected to poor growth at this thickness or specimen preparation issues. Certainly the latter is involved, as sample preparation led to damage in the lgr film too, leaving only a few nanometers near the interface (see Figure S11). The bulk film exhibits columnar epitaxial growth across the entire substrate surface. The substrate−film interface is easily found at low resolution, and there does not appear to be any lateral variation across the film. Further, the film contrast is relatively uniform through the thickness, when considering all regions. The film exhibits columnar contrast through the thickness, and dark/bright patches in the grains seem to be distributed uniformly, more likely from thickness or local strain effects than from different polymorphs.

A high-resolution image from the interfacial region is shown in Figure 6b. The substrate is on the bottom and columnar bulk on the top, with the interface between them. The interface normal is not in the plane of the image (i.e., the zone axis is not in the interface plane), and this leads to the interface spreading in the HR-TEM image. Nevertheless, there is good atom registry across the entire space. The columnar structure shows up as vertical contrast in the film region of the high-resolution TEM image. These vertical lines are narrowly spaced, much less than the specimen thickness; thus, they are likely distributed through the thickness.

The inset gives the SAED pattern from this interfacial region. There is only one set of spots, corresponding to the substrate (001) zone axis. It should be noted that the film repeat periods for the primary eutaxial OR of s-SnO_2 along this zone axis are 0.0 and −0.5% different from c-$CoNb_2O_6$ and that peak overlap is expected. The absence of other peaks supports the growth of s-SnO_2 having the primary eutaxial OR on this grain. Figure 6c,d gives the fast Fourier transform of the image for the film region (c) and substrate region (d). The substrate patterns have a tripling along [100], as expected for c-$CoNb_2O_6$, while the film patterns do not, as expected for s-SnO_2.

These observations support the assertion that s-SnO_2 grows on (100) c-$CoNb_2O_6$ and has the primary eutaxial OR. The observations from the lgr film (Figure S11) are also consistent with this observation (except for columnar growth). They also indicate that the growth of s-SnO_2 is relatively stable with respect to large changes in the growth rate on the (001) c-$CoNb_2O_6$ grains. In other words, the growth of s-SnO_2 on some orientations of c-$CoNb_2O_6$ is quite robust.

4. DISCUSSION

Using CSE, we generated several important findings for understanding polymorph competition during epitaxial nucleation and growth of metastable scrutinyite and stable rutile structured SnO_2 films on polycrystalline c-$CoNb_2O_6$. Essentially, both metastable s-SnO_2 and stable r-SnO_2 crystals are observed to grow, but each grows on specific ranges of substrate orientations, and each has a single specific orientation relationship (OR) with the substrate grain on which it grew. We discuss these observations further here.

Grain-over-grain epitaxial growth occurs for both s-SnO_2 and r-SnO_2 for all c-$CoNb_2O_6$ orientations. This means that surfaces of individual substrate grains (crystals) support the growth of a film having a very specific phase and orientation. Thus, each grain behaves as an independent crystal that supports epitaxial growth. In the late 1990s, Goyal et al. demonstrated that local epitaxial growth occurs for oxides on polycrystalline metals and oxides on polycrystalline oxides to engineer the grain boundaries in superconducting tapes.[65,66] Similarly, grain boundary magnetoresistance was investigated in locally epitaxial Sr_2FeMoO_6 double perovskites on polycrystalline $SrTiO_3$.[67] We have made similar observations in CSE growth of anatase and rutile TiO_2 on $BaTiO_3$,[56] and $BiFeO_3$,[57] Fe_2O_3 on $SrTiO_3$,[58] $BiFeO_3$ on $LaAlO_3$,[68] and Ca_2MnO_4 on Sr_2TiO_4,[59,60] $RE_2Ti_2O_7$ films on $Sr_2Nb_2O_7$,[25] and Sr_2FeMoO_6 on Sr_2MgWO_6.[69] Of course, such observations depend on the growth conditions and quality of the crystal surface. When EBSD patterns of the substrate are of good quality, the condition of good local surface quality is generally satisfied for *c*-$CoNb_2O_6$ (and other substrates[25,56−60,70]). The observation of grain-over-grain growth at relatively high growth rates reinforces this assertion. It is possible to further engineer the surfaces to obtain atomically flat surfaces on polycrystals, using standard methods carried out for single crystal surface engineering.[71] Of course, kinetic parameters are expected to affect growth in similar fashion to that on single crystal substrates, especially those with high step densities, which is to say in complex manners depending on the substrate−film pairs.

The high throughput method used to generate these observations hinges on the ability of automated indexing algorithms to properly assign orientations based on Kikuchi patterns. Standard commercial software was developed primarily for indexing the relatively simple structure of metals and alloys. Using CSE, we have demonstrated that this software can be properly deployed (by modifying input selectors) to map complex materials grown as thin films. However, subtle differences in structure should always cause concern for accurate orientation assignment. To verify the automated indexing with commercial software, we used an in-house program that simulates EBSD patterns of all orientations to generate a dictionary of patterns. Experimental patterns are then compared to the dictionary, and the one with the strongest correlation is accepted as the phase and orientation. This comparison does not require any user bias to the selection process and compares whole EBSD patterns, such that no information is ignored in the indexing process. Using this method, as shown in Figure 2, the dictionary method and the commercial software led to similar results. The dictionary approach offers several advantages, especially the lack of user-bias and the ability to compare experimental and best-fit simulation patterns. Further development is needed to use it routinely for the discrimination of patterns from similar structures.

Only one low-energy OR was found for either *s**-SnO_2 or *r*-SnO_2 with respect to the *c**-$CoNb_2O_6$ substrate grains, independent of the surface orientation. Having a small number of epitaxial ORs for any phase regardless of substrate orientation is a common observation in CSE experiments of epitaxial oxide growth[25,56−60,65−67] and is also usually true on low-index single crystals. For the metastable *s**-SnO_2 grains, this can be described as the unit-cell over unit-cell growth. This OR aligns the primary eutactic planes: $(100)_{s*}[001]_{s*}\|(100)_{c*}[001]_{c*}$, though any alignment of identical planes and directions would be an equally valid description of epitaxy. Considering the similarities of various orientations in the columbite and scrutinyite structures, it is at first surprising that a single OR is found. One could envision, when considering geometry alone, degenerate ORs of different eutactic planes. We discuss the origin of a single OR further with respect to phase selection, later.

For the stable *r*-SnO_2 grains, alignment of secondary pairs (see SI) of eutactic planes describes the OR: $\{101\}_r \langle 010_r\rangle \|(010)_{c*}[001]_{c*}$. Of course, one could write the OR using other planar alignments. For example, an equivalent description would be the alignment of the primary eutactic planes with an ~60° rotation about the plane normals from alignment of the [001] directions: or $\{100\}_r\langle 011\rangle_r\|(010)_{c*}[001]_{c*}$. The question is, which description is preferred. In the geology literature, it has been shown that epitaxial nanolayers form at rutile {101} twin boundaries[72−74] and that the scrutinyite structured TiO_2 (or TiO_2−II) adopted the same epitaxial relation with rutile as found here for rutile SnO_2 and columbite $CoNb_2O_6$. It was recognized that the $(101)_r$ and $(010)_{s*}$ planes are similar and that rutile {101} twins had scrutinyite structural character.[72−74] To illustrate this, schematics of the $(010)_{s*}$ *s*-SnO_2 and $(101)_r$ *r*-SnO_2 planes are given in Figure 7a,b and 7c,d, respectively. These two planes are strikingly similar to each other in both perspective views. Thus, describing epitaxy using this OR helps one understand the structural origin for its appearance and its stability near the $(010)_{c*}$ pole.

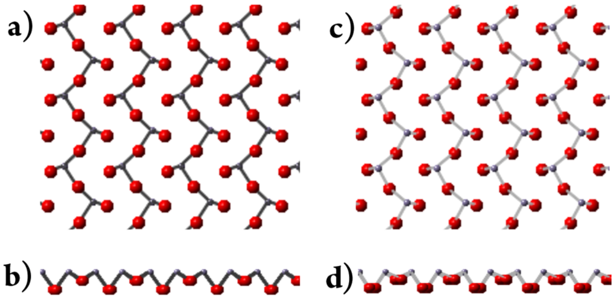

Figure 7. (a,b) The $(010)_{s*}$ plane of *s*-SnO_2. The *a*/*c* axes are horizontal/vertical in (a), and the *a*/*b* axes are horizontal (vertical) in (b). (c,d) The $(101)_r$ plane of *r*-SnO_2. The *b* axis/$[\mathbf{10\bar{1}}]_r$ direction are horizontal/vertical in (c), and *b* axis/$[\mathbf{101}]_r$ direction are horizontal/vertical in (d). Red (purple) spheres are O^{2-} anions (Sn^{4+} cations) and bonds are gray cylinders.[80]

A slight majority of *c**-$CoNb_2O_6$ orientations support the growth of the metastable *s**-SnO_2 polymorph, as observed in Figure 5. Similar observations were made for polymorph competition of anatase and rutile TiO_2 on perovskite surfaces using CSE[57,75] (in agreement with experiments on single crystals, as discussed in ref 29). The most likely origin of how a low number of ORs form, and how polymorph stability is a function of substrate orientation, is that surfaces of similar orientations are similar to one another. This is expected if the surfaces can be described using the terrace−ledge−kink (TLK) model,[76−79] where the surface of any orientation can be broken into three low-energy bounding surfaces of different areas. The terrace has the largest area, the ledge (or step) has the second largest area, and the kink has the least area of the bounding low-index surface.[76−79] Then, orientation space can be subdivided into regions bounded by different low energy TLK surfaces.[76−79] Within a specific region, the relative areas of TLKs vary smoothly. Because of this, surfaces across orientation space can be considered as being dominated by nucleation and growth events on low-index orientations, which is convenient in describing the energetics of epitaxial growth across orientation space.[29]

Using a first-principles model that considered three energetic terms, bulk volumetric, bulk strain, and film/substrate interfacial, Xu et al.[29] were able to reproduce the relative order of phase stability between anatase and rutile TiO_2 on perovskite surfaces. We describe the qualitative terms of interest for *s*-SnO_2 growth here. Mehta et al.[30] computed the bulk volumetric energy difference to be ~6 kJ/mol between *s*-SnO_2 and *r*-SnO_2,[30] well within the observed range for epitaxial stabilization (approximated therein as 20 kJ/mol, but which is very much dependent on film−substrate pairs).

The volumetric strain energies are related to the misfit epitaxial strains, which are straightforward to compute given crystal structures and low energy ORs. We have already demonstrated that two eutaxial ORs dominate for SnO_2 growth on columbite. In Table 1 (and Table S2), the misfit epitaxial strain terms are given for nine planar epitaxial ORs, for both *s**-SnO_2 and *r*-SnO_2

Table 1. Cation Stacking[a] and Epitaxial Strains[b,c] for the (Nearly) Eutaxial Planes of s^*-SnO_2[d] and r-SnO_2 on c^*-$CoNb_2O_6$[e]

Substrate	*Film*		
c^*-$CoNb_2O_6$		s^*-SnO_2	
	$\{100\}_{s^*}$ $[010]_{s^*}/[001]_{s^*}$	$\{010\}_{s^*}$ $[100]_{s^*}/[001]_{s^*}$	$\{012\}_{s^*}$ $[100]_{s^*}/[0 2 \bar{1}]_{s^*}$
$\{100\}_{c^*}$ $[010]_{c^*}/[001]_{c^*}$	$c_{1/2\text{-II}}$ / $c_{1/2\text{-II}}$ -3.4 / -0.5	$a_{1/4}c_{1/4\text{-I}}$ / $c_{1/2\text{-II}}$ +6.9 / -0.5	$a_{1/4}c_{1/4\text{-II}}$ / $c_{1/2\text{-II}}$ +6.9 / -4.2
$\{010\}_{c^*}$ $[100]_{c^*}/[001]_{c^*}$	$c_{1/2\text{-II}}$ / $a_{1/4}c_{1/4\text{-I}}$ -9.6 / -0.5	$a_{1/4}c_{1/4\text{-I}}$ / $a_{1/4}c_{1/4\text{-I}}$ 0.0 / -0.5	$a_{1/4}c_{1/4\text{-II}}$ / $a_{1/4}c_{1/4\text{-I}}$ 0.0 / -4.2
$\{012\}_{c^*}$ $[100]_{c^*}/[0 2 \bar{1}]_{c^*}$	$c_{1/2\text{-II}}$ / $a_{1/4}c_{1/4\text{-II}}$ -9.6 / +1.1	$a_{1/4}c_{1/4\text{-I}}$ / $a_{1/4}c_{1/4\text{-II}}$ 0.0 / +1.1	$a_{1/4}c_{1/4\text{-II}}$ / $a_{1/4}c_{1/4\text{-II}}$ 0.0 / -2.7
c^*-$CoNb_2O_6$		r-SnO_2	
	$\{100\}_r$ $[010]_r/[001]_r$	$\{010\}_r$ $[100]_r/[001]_r$	$\{101\}_r$ $[010]_r/[10\bar{1}]_r$
$\{100\}_{c^*}$ $[010]_{c^*}/[001]_{a^*}$	$c_{1/2\text{-I}}$ / $c_{1/2\text{-II}}$ +6.3 / -10.6	$c_{1/2\text{-I}}$ / $c_{1/2\text{-II}}$ +6.3 / -10.6	$a_{1/4}c_{1/4\text{-I}}$ / $c_{1/2\text{-II}}$ +6.3 / -0.2
$\{010\}_{a^*}$ $[100]_{c^*}/[001]_{c^*}$	$c_{1/2\text{-I}}$ / $a_{1/4}c_{1/4\text{-I}}$ -0.5 / -10.6	$c_{1/2}\text{-I}$ / $a_{1/4}c_{1/4\text{-I}}$ -0.5 / -10.6	$a_{1/4}c_{1/4\text{-I}}$ / $a_{1/4}c_{1/4\text{-I}}$ -0.5 / -0.2
$\{012\}_{c^*}$ $[100]_{c^*}/[0 2 \bar{1}]_{c^*}$	$c_{1/2\text{-I}}$ / $a_{1/4}c_{1/4\text{-II}}$ -0.5 / -9.2	$c_{1/2\text{-I}}$ / $a_{1/4}c_{1/4\text{-II}}$ -0.5 / -9.2	$a_{1/4}c_{1/4\text{-I}}$ / $a_{1/4}c_{1/4\text{-II}}$ -0.5 / +1.4

[a] Written as film/substrate pairs using notation described in §S1–S3. [b] See Tables S1 for values. [c] All units are in % determined by $(d_{subs} - d_{film})/d_{film} \times 100$. [d] s^*-SnO_2 is described using a *Pcnb* scrutinyite unit cell. [e] c^*-$CoNb_2O_6$ is given for a scrutinyite unit cell, with no tripling.

on c^*-$CoNb_2O_6$ (and r-SnO_2 on s^*-SnO_2 to model persistent nucleation), as well as (Table S2) for the expected OR for the noneutaxial bounding plane (001). Distances used in these calculations are given in the SI (Table S1). Epitaxial strain values less than 4% are highlighted.

For s^*-SnO_2, the unit-cell over unit-cell ORs (the diagonal terms in Table 1 and the lowest left in Table S2), all have a low strain energy. However, so does the alignment of the $\{010\}_{s^*}$ planes of s^*-SnO_2 with the $\{012\}_{s^*}$ planes in c^*-$CoNb_2O_6$; in fact, these strain terms are second lowest in Table 1 for s^*-SnO_2, but this OR is not observed. For r-SnO_2, the observed OR has the lowest strain energy, but an OR that aligns the $\{101\}_r$ and $\{012\}_{s^*}$ is also relatively low in strain energy. If the observation of single ORs is explained by only attaining the lowest strain energy terms, the alignment of $\{010\}_{s^*}$ planes for s^*-SnO_2 and c^*-$CoNb_2O_6$ leads to a potential epitaxial OR. Unfortunately, rutile SnO_2 dominates growth on the $\{010\}_{s^*}$ surface. Also, on the $\{012\}_{s^*}$ surface, one expects strain to prefer the $\{010\}_{s^*}$ OR alignment, but this is not observed. This is either a result of the $\{012\}_{s^*}$ surface having little influence in the TLK surface, which is not known (see §S4 for low energy surface planes), or interfacial energy terms being important.

The interfacial energy penalties are associated with the cation packing differences within given low index planes. In Table 1, the cation packing pairs for specific ORs are also given (notation is described in §S1–S3). Whenever the cation packing is identical, the cell is highlighted in Table 1 (i.e., $c_{1/2\text{-}II}/c_{1/2\text{-}II}$ for alignment of $\{100\}_{s^*}$ planes in s^*-SnO_2 and c^*-$CoNb_2O_6$). When considering the cation packing differences, which result in interfacial energy penalties similar to stacking fault or twin boundary penalties, the observed ORs are immediately distinguishable from the low strain energy competitors that were not observed. In fact, the observed ORs are those that minimize strain energy and have identical cation packing to minimize interfacial terms. Of course, when both s-SnO_2 and r-SnO_2 are similarly competitive in the strain and interface terms, as on $\{010\}_{s^*}$ c-$CoNb_2O_6$, rutile wins the competition owing to its bulk stability. However, in regions of orientation space where the $\{010\}_{s^*}$ becomes unimportant in the TLK surface structure, the combination of large strains and interfacial cation packing mismatch destabilizes the rutile polymorph and allows for the appearance of epitaxial growth of metastable s-SnO_2.

Collectively, the observations made for polymorph competition during CSE growth of SnO_2 on c-$CoNb_2O_6$ are very promising to develop new materials by epitaxy. Because the few ORs observed for each phase were readily described qualitatively using bulk, strain, and interface terms, growth competitions of rutile and scrutinyite structured oxides should be nearly ideal to explore computationally guided synthesis using first principles.[29] Combining computational predictions of properties, such as improved catalytic performance of scrutinyite structured IrO_2,[48] with an ability to predict synthesis pathways[29] could greatly accelerate new materials fabrication. Of most interest is how the cation packing penalties vary as a function of cation. This could be used to tune substrates and will ultimately bound which materials can be stabilized and which cannot.

5. CONCLUSIONS

We used combinatorial substrate epitaxy (CSE) to investigate polymorph competition between metastable scrutinyite (α-PbO_2) structured and stable rutile structured SnO_2 during epitaxial growth on polycrystalline c-$CoNb_2O_6$ substrates. Growth occurs in a grain-over-grain fashion, where each grain of the substrate supports the growth of a grain in the film with a single OR. Both metastable s-SnO_2 and stable r-SnO_2 crystals are observed, but each grows on specific ranges of substrate orientations and each has a single OR with the substrate grain on which it grew. The collected set of observations is discussed and rationalized with respect to the combination of misfit strain energies and cation packing interfacial energy penalties. We conclude that CSE should allow for the rational and computationally guided development of new materials adopting scutinyite, rutile, and related structures.

■ ASSOCIATED CONTENT

Ⓢ Supporting Information

The Supporting Information is available free of charge on the ACS Publications website at DOI: 10.1021/acs.cgd.7b00569.

> Descriptions and schematic images of rutile, scrutinyite, and columbite crystal structures, including important crystallographic planes relative to structure, energy, and symmetry. Supporting Tables for the potential epitaxial ORs. Raw IPF maps associated with Figures 1 and 3. Description of parameters used in simulations and dictionary indexing of EBSD patterns (shown in Figure 2). Large-area IPF maps and determination epitaxial ORs are shown for the hgr samples (whose TEM images are given in Figure 6). IPF maps from the grains used for TEM specimen preparation and TEM results from the lgr sample (PDF)

AUTHOR INFORMATION

Corresponding Author

*Email: paulsalvador@cmu.edu.

ORCID

Zhongnan Xu: 0000-0002-6930-2360
John R. Kitchin: 0000-0003-2625-9232
Gregory S. Rohrer: 0000-0002-9671-3034
Paul A. Salvador: 0000-0001-7106-0017

Present Address

[§]Boopathy Kombaiah, Oak Ridge National Laboratory, P.O. Box 2008, Oak Ridge, Tennessee 37831-6138, United States.

Author Contributions

The manuscript was written through contributions of all authors. All authors have given approval to the final version of the manuscript.

Notes

The authors declare no competing financial interest.

ACKNOWLEDGMENTS

J.W., P.A.S., and G.S.R. acknowledge the support of the National Science Foundation: grant DMR 1609355. F.R. and M.D.G. acknowledge the support of the Air Force Office of Scientific Research (AFOSR): MURI program, contract # FA9550-12-1-0458. The authors acknowledge use of the Materials Characterization Facility at Carnegie Mellon University, supported by grant MCF-677785.

ABBREVIATIONS

c-, columbite-structured; *c**, columbite in an *s** subcell; CSE, combinatorial substrate epitaxy; EBSD, electron backscatter diffraction; FIB, focused ion beam; hcp, hexagonal close-packed; hgr, high growth rate; IPF, inverse pole figure; IQ, image quality; *lgr*, low growth rate; OR, orientation relationship; *r*-, rutile-structured; *s*-, scrutinyite-structured; *s**, scrutinyite in *Pcnb* setting; SAED, selected-area electron diffraction; SEM, scanning electron microscopy; SI, Supporting Information; TEM, transmission electron microscopy; TLK, terrace-ledge-kink

REFERENCES

(1) Disalvo, F. J. Solid-State Chemistry - a Rediscovered Chemical Frontier. *Science* **1990**, *247*, 649−655.

(2) Gopalakrishnan, J. Chimie Douce Approaches to the Synthesis of Metastable Oxide Materials. *Chem. Mater.* **1995**, *7*, 1265−1275.

(3) Price, S. L. Why don't we find more polymorphs? *Acta Crystallogr., Sect. B: Struct. Sci., Cryst. Eng. Mater.* **2013**, *69*, 313−328.

(4) Jansen, M. A concept for synthesis planning in solid-state chemistry. *Angew. Chem., Int. Ed.* **2002**, *41*, 3746−3766.

(5) Sun, W.; Dacek, S. T.; Ong, S. P.; Hautier, G.; Jain, A.; Richards, W. D.; Gamst, A. C.; Persson, K. A.; Ceder, G. The thermodynamic scale of inorganic crystalline metastability. *Science Advances* **2016**, *2*, e1600225.

(6) Zhang, H. Z.; Banfield, J. F. Understanding polymorphic phase transformation behavior during growth of nanocrystalline aggregates: Insights from TiO_2. *J. Phys. Chem. B* **2000**, *104*, 3481−3487.

(7) McMillan, P. F. New materials from high-pressure experiments. *Nat. Mater.* **2002**, *1*, 19−25.

(8) Das, S.; Jayaraman, V. SnO_2: A comprehensive review on structures and gas sensors. *Prog. Mater. Sci.* **2014**, *66*, 112−255.

(9) Karki, B. B.; Warren, M. C.; Stixrude, L.; Ackland, G. J.; Crain, J. Ab initio studies of high-pressure structural transformations in silica. *Phys. Rev. B: Condens. Matter Mater. Phys.* **1997**, *55*, 3465−3471.

(10) Tsuchiya, J.; Tsuchiya, T.; Wentzcovitch, R. M. Transition from the Rh_2O_3(II)-to-$CaIrO_3$ structure and the high-pressure-temperature phase diagram of alumina. *Phys. Rev. B: Condens. Matter Mater. Phys.* **2005**, *72*, 020103.

(11) Dubrovinskaia, N.; Dubrovinsky, L.; Ahuja, R.; Prokopenko, V.; Dmitriev, V.; Weber, H. P.; Osorio-Guillen, J.; Johansson, B. Experimental and Theoretical Identification of a New High-Pressure TiO_2 Polymorph. *Phys. Rev. Lett.* **2001**, *87*, 275501.

(12) Gracia, L.; Beltran, A.; Andres, J. Characterization of the high-pressure structures and phase transformations in SnO_2. A density functional theory study. *J. Phys. Chem. B* **2007**, *111*, 6479−6485.

(13) Erdem, I.; Kart, H. H.; Cagin, T. High pressure phase transitions in SnO_2 polymorphs by first-principles calculations. *J. Alloys Compd.* **2014**, *587*, 638−645.

(14) Barnard, A. S.; Zapol, P. A model for the phase stability of arbitrary nanoparticles as a function of size and shape. *J. Chem. Phys.* **2004**, *121*, 4276−4283.

(15) Barnard, A. S.; Zapol, P. Effects of particle morphology and surface hydrogenation on the phase stability of TiO_2. *Phys. Rev. B: Condens. Matter Mater. Phys.* **2004**, *70*, 235403.

(16) Levchenko, A. A.; Li, G. S.; Boerio-Goates, J.; Woodfield, B. F.; Navrotsky, A. TiO_2 stability landscape: Polymorphism, surface energy, and bound water energetics. *Chem. Mater.* **2006**, *18*, 6324−6332.

(17) Castro, R. H. R.; Wang, B. B. The Hidden Effect of Interface Energies in the Polymorphic Stability of Nanocrystalline Titanium Dioxide. *J. Am. Ceram. Soc.* **2011**, *94*, 918−924.

(18) Wang, C. C.; Ying, J. Y. Sol-gel synthesis and hydrothermal processing of anatase and rutile titania nanocrystals. *Chem. Mater.* **1999**, *11*, 3113−3120.

(19) Zhang, H. Z.; Banfield, J. F. Thermodynamic analysis of phase stability of nanocrystalline titania. *J. Mater. Chem.* **1998**, *8*, 2073−2076.

(20) Gorbenko, O. Y.; Samoilenkov, S. V.; Graboy, I. E.; Kaul, A. R. Epitaxial stabilization of oxides in thin films. *Chem. Mater.* **2002**, *14*, 4026−4043.

(21) Schlom, D. G.; Chen, L.-Q.; Pan, X.; Schmehl, A.; Zurbuchen, M. A. A thin film approach to engineering functionality into oxides. *J. Am. Ceram. Soc.* **2008**, *91*, 2429−2454.

(22) Mercey, B.; Salvador, P. A.; Prellier, W.; Doan, T.-D.; Wolfman, J.; Hervieu, M.; Raveau, B. Thin film deposition: a novel synthetic route to new materials. *J. Mater. Chem.* **1999**, *9*, 233−242.

(23) Chambers, S. A. Epitaxial Growth and Properties of Doped Transition Metal and Complex Oxide Films. *Adv. Mater.* **2010**, *22*, 219−248.

(24) Lowndes, D. H.; Geohegan, D. B.; Puretzky, A. A.; Norton, D. P.; Rouleau, C. M. Synthesis of novel thin-film materials by pulsed laser deposition. *Science* **1996**, *273*, 898−903.

(25) Havelia, S.; Wang, S.; Balasubramaniam, K. R.; Schultz, A. M.; Rohrer, G. S.; Salvador, P. A. Combinatorial substrate epitaxy: a new approach to growth of complex metastable compounds. *CrystEngComm* **2013**, *15*, 5434−5441.

(26) Havelia, S.; Wang, S.; Balasubramaniam, K. R.; Salvador, P. A. Thin Film Synthesis and Structural Characterization of a New Kinetically Preferred Polymorph in the $RE_2Ti_2O_7$ (RE = La-Y) Family. *Cryst. Growth Des.* **2009**, *9*, 4546−4554.

(27) Salvador, P. A.; Doan, T. D.; Mercey, B.; Raveau, B. Stabilization of $YMnO_3$ in a perovskite structure as a thin film. *Chem. Mater.* **1998**, *10*, 2592−2595.

(28) Balasubramaniam, K. R.; Havelia, S.; Salvador, P. A.; Zheng, H.; Mitchell, J. F. Epitaxial stabilization and structural properties of $REMnO_3$ (RE = Dy,Gd,Sm) compounds in a layered, hexagonal ABO3 structure. *Appl. Phys. Lett.* **2007**, *91*, 232901.

(29) Xu, Z.; Salvador, P. A.; Kitchin, J. R. First-Principles Investigation of the Epitaxial Stabilization of Oxide Polymorphs: TiO_2 on (Sr/Ba)TiO_3. *ACS Appl. Mater. Interfaces* **2017**, *9*, 4106−4118.

(30) Mehta, P.; Salvador, P. A.; Kitchin, J. R. Identifying Potential BO_2 Oxide Polymorphs for Epitaxial Growth Candidates. *ACS Appl. Mater. Interfaces* **2014**, *6*, 3630−3639.

(31) Mathew, K.; Singh, A. K.; Gabriel, J. J.; Choudhary, K.; Sinnott, S. B.; Davydov, A. V.; Tavazza, F.; Hennig, R. G. MPInterfaces: A Materials Project based Python tool for high-throughput computational screening of interfacial systems. *Comput. Mater. Sci.* **2016**, *122*, 183−190.

(32) Ding, H.; Dwaraknath, S. S.; Garten, L.; Ndione, P.; Ginley, D.; Persson, K. A. Computational Approach for Epitaxial Polymorph Stabilization through Substrate Selection. *ACS Appl. Mater. Interfaces* **2016**, *8*, 13086−13093.

(33) Posadas, A.; Yau, J. B.; Ahn, C. H.; Han, J.; Gariglio, S.; Johnston, K.; Rabe, K. M.; Neaton, J. B. Epitaxial growth of multiferroic $YMnO_3$ on GaN. *Appl. Phys. Lett.* **2005**, *87*, 171915.

(34) Batzill, M.; Diebold, U. The surface and materials science of tin oxide. *Prog. Surf. Sci.* **2005**, *79*, 47−154.

(35) Wang, Y.; Lee, J. Y.; Zeng, H. C. Polycrystalline SnO_2 nanotubes prepared via infiltration casting of nanocrystallites and their electrochemical application. *Chem. Mater.* **2005**, *17*, 3899−3903.

(36) Kowal, A.; Li, M.; Shao, M.; Sasaki, K.; Vukmirovic, M. B.; Zhang, J.; Marinkovic, N. S.; Liu, P.; Frenkel, A. I.; Adzic, R. R. Ternary Pt/Rh/SnO_2 electrocatalysts for oxidizing ethanol to CO_2. *Nat. Mater.* **2009**, *8*, 325−330.

(37) Suito, K.; Kawai, N.; Masuda, Y. High-Pressure Synthesis of Orthorhombic SnO_2. *Mater. Res. Bull.* **1975**, *10*, 677−680.

(38) Haines, J.; Leger, J. M. X-ray diffraction study of the phase transitions and structural evolution of tin dioxide at high pressure: Relationships between structure types and implications for other rutile-type dioxides. *Phys. Rev. B: Condens. Matter Mater. Phys.* **1997**, *55*, 11144−11154.

(39) Dai, Z. R.; Gole, J. L.; Stout, J. D.; Wang, Z. L. Tin oxide nanowires, nanoribbons, and nanotubes. *J. Phys. Chem. B* **2002**, *106*, 1274−1279.

(40) Shin, J. H.; Park, H. M.; Song, J. Y. Phase transformation of hierarchical nanobranch structure from SnO to SnO_2 and its electrochemical capacitance. *J. Alloys Compd.* **2013**, *551*, 451−455.

(41) Bae, J. Y.; Park, J.; Kim, H. Y.; Kim, H. S.; Park, J. S. Facile Route to the Controlled Synthesis of Tetragonal and Orthorhombic SnO_2 Films by Mist Chemical Vapor Deposition. *ACS Appl. Mater. Interfaces* **2015**, *7*, 12074−12079.

(42) Kong, L. Y.; Ma, J.; Luan, C. N.; Zhu, Z. Structural and optical properties of single crystalline columbite tin oxide film. *Appl. Phys. Lett.* **2011**, *98*, 261904.

(43) Kong, L. Y.; Ma, J.; Zhu, Z.; Luan, C. N.; Yu, X. H.; Yu, Q. Q. Synthesis of orthorhombic structure epitaxial tin oxide film. *Mater. Lett.* **2010**, *64*, 1350−1353.

(44) Kong, L. Y.; Ma, J.; Zhu, Z.; Luan, C. N.; Ji, F. Structural, electrical and optical properties of SnO_2 films deposited on Y-stabilized ZrO_2 (100) substrates by MOCVD. *J. Cryst. Growth* **2010**, *312*, 2931−2935.

(45) Sangaletti, L.; Depero, L. E.; Dieguez, A.; Marca, G.; Romano-Rodriguez, A.; Sberveglieri, G.; Morante, J. R. Microstructure and morphology of tin dioxide multilayer thin film gas sensors. *Sens. Actuators, B* **1997**, *44*, 268−274.

(46) Kim, S.; Kim, D.; Hong, S.-H. Epitaxial growth of orthorhombic SnO_2 films on various YSZ substrates by plasma enhanced atomic layer deposition. *J. Cryst. Growth* **2012**, *348*, 15−19.

(47) Haines, J.; Leger, J. M. Phase transitions in ruthenium dioxide up to 40 GPa: Mechanism for the rutile-to-fluorite phase transformation and a model for the high-pressure behavior of stishovite SiO_2. *Phys. Rev. B: Condens. Matter Mater. Phys.* **1993**, *48*, 13344−13350.

(48) Xu, Z.; Kitchin, J. R. Tuning oxide activity through modification of the crystal and electronic structure: from strain to potential polymorphs. *Phys. Chem. Chem. Phys.* **2015**, *17*, 28943−28949.

(49) O'Keeffe, M. On the arrangements of ions in crystals. *Acta Crystallogr., Sect. A: Cryst. Phys., Diffr., Theor. Gen. Crystallogr.* **1977**, *33*, 924−927.

(50) Rohrer, G. S. *Structure and Bonding in Crystalline Materials*; Cambridge University Press, 2004; p 540.

(51) Pullar, R. C. The Synthesis, Properties, and Applications of Columbite Niobates ($M^{2+}Nb_2O_6$): A Critical Review. *J. Am. Ceram. Soc.* **2009**, *92*, 563−577.

(52) Sturdivant, J. H. The crystal structure of columbite. *Z. Kristallogr. - Cryst. Mater.* **1930**, *75*, 88−108.

(53) Arroyo y de Dompablo, M. E.; Lee, Y. L.; Morgan, D. First Principles Investigation of Oxygen Vacancies in Columbite MNb_2O_6 (M = Mn, Fe, Co, Ni, Cu). *Chem. Mater.* **2010**, *22*, 906−913.

(54) Husson, E.; Repelin, Y.; Dao, N. Q.; Brusset, H. Characterization of Different Bondings in Some Divalent Metal Niobates of Columbite Structure. *Mater. Res. Bull.* **1977**, *12*, 1199−1206.

(55) $CoNb_2O_6$ (Nb_2CoO_6 orth) Crystal Structure: http://materials.springer.com/isp/crystallographic/docs/sd_0378256. In *PAULING FILE: Inorganic Solid Phases, SpringerMaterials (online database)*; Villars, P., Ed.; Springer-Verlag GmbH: 2016.

(56) Burbure, N. V.; Salvador, P. A.; Rohrer, G. S. Orientation and phase relationships between titania films and polycrystalline $BaTiO_3$ substrates as determined by electron backscatter diffraction mapping. *J. Am. Ceram. Soc.* **2010**, *93*, 2530−2533.

(57) Zhang, Y.; Schultz, A. M.; Li, L.; Chien, H.; Salvador, P. A.; Rohrer, G. S. Combinatorial Substrate Epitaxy: A high throughput method for determining phase and orientation relationships and its application to $BiFeO_3/TiO_2$ heterostructures. *Acta Mater.* **2012**, *60*, 6486−6493.

(58) Schultz, A. M.; Zhu, Y.; Bojarski, S. A.; Rohrer, G. S.; Salvador, P. A. Eutaxial growth of hematite Fe_2O_3 films on perovskite $SrTiO_3$ polycrystalline substrates. *Thin Solid Films* **2013**, *548*, 220−224.

(59) Lacotte, M.; David, A.; Pravarthana, D.; Grygiel, C.; Rohrer, G. S.; Salvador, P. A.; Velazquez, M.; de Kloe, R.; Prellier, W. Growth of Ca_2MnO_4 Ruddlesden-Popper structured thin films using Combinatorial Substrate Epitaxy. *J. Appl. Phys.* **2014**, *116*, 245303.

(60) Lacotte, M.; David, A.; Rohrer, G. S.; Salvador, P. A.; Prellier, W. Preferential Orientation Relationships in Ca_2MnO_4 Ruddlesden-Popper thin films. *J. Appl. Phys.* **2015**, *118*, 045306.

(61) Lorenz, M.; Ramachandra Rao, M. S.; Venkatesan, T.; Fortunato, E.; Barquinha, P.; Branquinho, R.; Salgueiro, D.; Martins, R.; Carlos, E.; Liu, A.; Shan, F. K.; Grundmann, M.; Boschker, H.; Mukherjee, J.; Priyadarshini, M.; DasGupta, N.; Rogers, D. J.; Teherani, F. H.; Sandana, E. V.; Bove, P.; Rietwyk, K.; Zaban, A.; Veziridis, A.; Weidenkaff, A.; Muralidhar, M.; Murakami, M.; Abel, S.; Fompeyrine, J.; Zuniga-Perez, J.; Ramesh, R.; Spaldin, N. A.; Ostanin, S.; Borisov, V.; Mertig, I.; Lazenka, V.; Srinivasan, G.; Prellier, W.; Uchida, M.; Kawasaki, M.; Pentcheva, R.; Gegenwart, P.; Miletto Granozio, F.; Fontcuberta, J.; Pryds, N. The 2016 oxide electronic materials and oxide interfaces roadmap. *J. Phys. D: Appl. Phys.* **2016**, *49*, 433001.

(62) Callahan, P. G.; De Graef, M. Dynamical Electron Backscatter Diffraction Patterns. Part I: Pattern Simulations. *Microsc. Microanal.* **2013**, *19*, 1255−1265.

(63) Chen, Y. H.; Park, S. U.; Wei, D.; Newstadt, G.; Jackson, M. A.; Simmons, J. P.; De Graef, M.; Hero, A. O. A Dictionary Approach to Electron Backscatter Diffraction Indexing. *Microsc. Microanal.* **2015**, *21*, 739−752.

(64) Singh, S.; De Graef, M. Orientation sampling for dictionary-based diffraction pattern indexing methods. *Modell. Simul. Mater. Sci. Eng.* **2016**, *24*, 085013.

(65) Goyal, A.; Paranthaman, M. P.; Schoop, U. The RABiTS approach: Using rolling-assisted biaxially textured substrates for high-performance YBCO superconductors. *MRS Bull.* **2004**, *29*, 552−561.

(66) Goyal, A.; Norton, D. P.; Kroeger, D. M.; Christen, D. K.; Paranthaman, M.; Specht, E. D.; Budai, J. D.; He, Q.; Saffian, B.; List, F. A.; Lee, D. F.; Hatfield, E.; Martin, P. M.; Klabunde, C. E.; Mathis, J.; Park, C. Conductors With Controlled Grain Boundaries: An Approach to the Next Generation, High Temperature Superconducting Wire. *J. Mater. Res.* **1997**, *12*, 2924−2940.

(67) Shinde, S. R.; Ogale, S. B.; Greene, R. L.; Venkatesan, T.; Tsoi, K.; Cheong, S. W.; Millis, A. J. Thin films of double perovskite Sr_2FeMoO_6: Growth, optimization, and study of the physical and magnetotransport properties of films grown on single-crystalline and polycrystalline $SrTiO_3$ substrates. *J. Appl. Phys.* **2003**, *93*, 1605−1612.

(68) Pravarthana, D.; Trassin, M.; Haw Chu, J.; Lacotte, M.; David, A.; Ramesh, R.; Salvador, P. A.; Prellier, W. $BiFeO_3/La_{0.7}Sr_{0.3}MnO_3$ Heterostructures deposited on Spark Plasma Sintered $LaAlO_3$ Substrates. *Appl. Phys. Lett.* **2014**, *104*, 082914.

(69) Santosh, M.; Lacotte, M.; David, A.; Boullay, P.; Grygiel, C.; Pravarthana, D.; Rohrer, G. S.; Salvador, P. A.; Padhan, P.; Luders, U.; Wang, J. L.; Prellier, W. Pulsed laser deposition of Sr2FeMoO6 thin

films grown on spark plasma sintered Sr2MgWO6 substrates. *J. Phys. D: Appl. Phys.* **2017**, *50*, 235301.

(70) Pravarthana, D.; Lebedev, O. I.; Hebert, S.; Chateigner, D.; Salvador, P. A.; Prellier, W. High-throughput synthesis of thermoelectric $Ca_3Co_4O_9$ films. *Appl. Phys. Lett.* **2013**, *103*, 143123.

(71) Woo, S.; Jeong, H.; Lee, S. A.; Seo, H.; Lacotte, M.; David, A.; Kim, H. Y.; Prellier, W.; Kim, Y.; Choi, W. S. Surface properties of atomically flat poly-crystalline $SrTiO_3$. *Sci. Rep.* **2015**, *5*, 8822.

(72) Hwang, S. L.; Shen, P. Y.; Chu, H. T.; Yui, T. F. Nanometer-size alpha-PbO_2-type TiO_2 in garnet: A thermobarometer for ultrahigh-pressure metamorphism. *Science* **2000**, *288*, 321−324.

(73) Wu, X. L.; Meng, D. W.; Han, Y. J. alpha-PbO_2-type nanophase of TiO_2 from coesite-bearing eclogite in the Dabie Mountains, China - Reply. *Am. Mineral.* **2006**, *91*, 1701−1702.

(74) Meng, D. W.; Wu, X. L.; Sun, F.; Huang, L. W.; Liu, F.; Han, Y. J.; Zheng, J. P.; Meng, X.; Mason, R. High-pressure polymorphic transformation of rutile to alpha-PbO_2-type TiO_2 at {011}(R) twin boundaries. *Micron* **2008**, *39*, 280−286.

(75) Burbure, N. V.; Salvador, P. A.; Rohrer, G. S. Orientation and Phase Relationships between Titania Films and Polycrystalline $BaTiO_3$ Substrates as Determined by Electron Backscatter Diffraction Mapping. *J. Am. Ceram. Soc.* **2010**, *93*, 2530−2533.

(76) Sholl, D. S.; Asthagiri, A.; Power, T. D. Naturally chiral metal surfaces as enantiospecific adsorbents. *J. Phys. Chem. B* **2001**, *105*, 4771−4782.

(77) Gruber, E. E.; Mullins, W. W. On the theory of anisotropy of crystalline surface tension. *J. Phys. Chem. Solids* **1967**, *28*, 875−887.

(78) Mackenzie, J. K.; Nicholas, J. F. Bonds broken at atomically flat crystal surfaces—II. *J. Phys. Chem. Solids* **1962**, *23*, 197−205.

(79) Mackenzie, J. K.; Moore, A. J. W.; Nicholas, J. F. Bonds broken at atomically flat crystal surfaces—I. *J. Phys. Chem. Solids* **1962**, *23*, 185−196.

(80) Images generated and distances/angles calcuated using *CrystalMaker* (v. 9.2.6): a crystal and molecular structures program for Mac and Windows; CrystalMaker Software Ltd.: Oxford, England, 2016.

Supporting Information: Competitive Growth of Scrutinyite (α-PbO_2) and Rutile Polymorphs of SnO_2 on All Orientations of Columbite $CoNb_2O_6$ Substrates

Julia Wittkamper,[†] Zhongnan Xu,[‡] Boopathy Kombaiah,[†,§] Farangis Ram,[†] Marc De Graef,[†] John R. Kitchin,[‡] Gregory S. Rohrer,[†] Paul A. Salvador[†,*]

[†] Department of Materials Science and Engineering, Carnegie Mellon University, 5000 Forbes Ave, Pittsburgh, PA 15213

[‡] Department of Chemical Engineering, Carnegie Mellon University, 5000 Forbes Ave, Pittsburgh, PA 15213* paulsalvador@cmu.edu

ABSTRACT: This document provides supporting information to the main text. The sections are as follows. Descriptions of the rutile (§S1) and scrutinyite (§S2), or α-PbO_2, polymorphs and depictions of the idealized structures of important planes (Figure S1, S2, and S3). §S3. A description of the columbite structure as related to scrutinyite. §S4. A description of the important crystallographic planes relative to structure, energy, and symmetry. §S5. A discussion of the standard stereographic projections (Figure S4) for tetragonal rutile and orthorhombic scrutinyite, and the relationships between them. §S6. A description of potential epitaxial orientation relationships (*ORs*) along with important periodic repeats (Table S1) and potential interfacial stacking faults and misfit strains (Table S2) that are not given in Table 1 of the main text. §S7. High resolution raw *IPF* maps (Figure S5) and image quality *IQ* maps (Figure S6) from the low growth rate (*lgr*) sample; the cleaned *IPF* maps are given in Figure 1 in the main text. §S8. A description of parameters used in simulations and dictionary indexing of *EBSD* patterns (shown in Figure 2 of the main text). §S9. Raw large area *IPF* maps (Figure S7) from the *lgr* sample; the cleaned *IPF* maps are shown in Figure 3 of the main text. §S10. Cleaned large-area *IPF* maps, Figure S8, from the high-growth rate (*hgr*) sample; only *TEM* images from the *hgr* sample are given in the main text (Figure 6). §S11. Demonstration of the epitaxial ORs in the *hgr* samples (Figure S9). §S12. *IPF* maps from the grains used for *TEM* specimen preparation (Figure S10). §S13. *TEM* results from the *lgr* sample (Figure S11); *TEM* from the *hgr* sample are given in Figure 6 of the main text.

S1. RUTILE STRUCTURE

The rutile (*r*) crystal structure of SnO_2 is tetragonal, has the space group $P4_2/mnm$ (No. 136), and has lattice parameters $\mathbf{a_r}$ = 4.737 and $\mathbf{c_r}$ = 3.186 Å.[1] The fractional positions of the oxide ion (O^{2-}) are 0.306, 0.306, 0 and of the tetravalent tin (Sn^{4+}) are 0, 0, 0.[1] The oxide anions can be considered as a eutactic network (nearly close-packed) with $(100)_r$ as the primary eutactic plane and stacking along $[100]_r$ being hexagonal close-packed (*hcp*).[2] In other words, they stack in so-called …ABAB… fashion (the upper case letters denote anion positions). Figure S1(a) shows one eutactic $(100)_r$ plane of oxygen and tin ions in *r*-SnO_2. It should be noted that the eutactic planes are significantly distorted in rutile,[3] with atom displacements in and out of the eutactic plane, resulting in the observed tetragonal symmetry. Rutile stacking can also be described as tetragonal stacking,[3] a variant of *hcp* related to these distortions. The result of the tetragonal stacking is that the crystal becomes tetragonal and that the $(010)_r$ planes, 90 ° away from the $(100)_r$, are crystallographically equivalent primary eutactic planes.

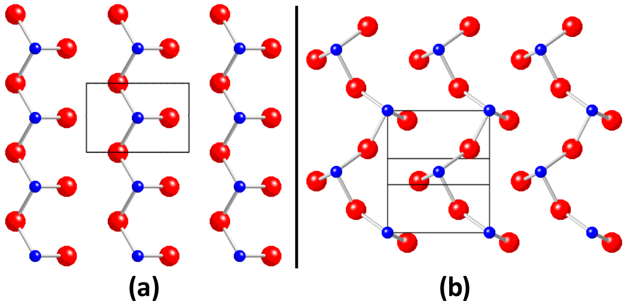

Figure S1. (a) The $(100)_r$ plane of rutile (*r*) SnO_2. The **b** (**c**) axis is horizontal (vertical). (b) The $(101)_r$ plane of *r*-SnO_2. The **b** axis ($[10\bar{1}]_r$ direction) is horizontal (vertical). Red (blue) spheres are O^{2-} anions (Sn^{4+} cations) and bonds are white cylinders.[6]

The tin cations occupy octahedral interstices in the eutactic network. The octahedral sites can be written as *c* in the stacking sequence …AcBcAcB… There is 1 octahedral interstice (*c*) per oxide ion in the eutactic network, but only ½ of them are filled by tin cations owing to the formula SnO_2. In the $(100)_r$ eutactic plane of *r*-SnO_2, the tin cations fill every other row of interstices running along $[001]_r$ (vertically in Figure S1(a)). This pattern we call $c_{½\text{-}I}$ (which is equivalent to the XY-I nomenclature by Morris[4, 5]). In the tetragonal packing description, the filled octahedral sites are the (relatively) undistorted octahedral sites. Note that the cations are slightly displaced away from the *c*-column of the true *hcp* stacking, away from one anion and towards the center between the other two anions in the plane below. Ultimately, we can write the structure as $\ldots \mathrm{A}c_{½\text{-}I}Bc_{½\text{-}I}\,\mathrm{A}c_{½\text{-}I}B\ldots$

A further consequence of the distorted *hcp* (or tetragonal packing) is that the anions in the $\{101\}_r$ planes have a similar structure to the eutactic $\{100\}_{\mathrm{r}}$ planes, but are more distorted from an apparent hexagonal net. Figure S1(b) shows an $(101)_r$ plane of oxygen and tin ions in *r*-SnO_2. The significant distortions away from a true eutactic hexagonal plane are immediately evident in this plane, and there are severe displacement out of the plane too. Despite these severe distortions, one can use close-packed terms to describe the structure, and we do so for simplicity and comparison sake to scrutinyite. We can again describe the structure along this direction as …ABAB... stacking, with the significant distortions noted.

Describing the cations in the secondary eutactic $(101)_r$ plane using the eutactic description is more tenuous. The cations above an A (B) plane occupy ¼ of the *c* and *a* sites (*c* and *b* sites), in a stacking we call $\ldots \mathrm{A}a_{¼}c_{¼\text{-}I}\mathrm{B}b_{¼}c_{¼\text{-}I}\ldots$ While in true *hcp* these would be octahedral and tetrahedral sites, respectively, in the distorted $(101)_r$ planes they are all octahedrally coordinated (there are more octahedral sites in tetragonal packing than in *hcp*[3]). That they are octahedral is evident in that each cation is bonded to three anions below their plane. That they are distorted from *hcp* is evident from the cations being severely moved away from the center point above those three anions (they tend to be located directly above the line between two cations, but remember the planes are severely buckled). Considering the bond connectivity of cations above an *A* plane, tin cations fill ½ of every other *c* and *a* rows running along the $[10\bar{1}]_r$ (vertical in Figure S1(b)), while the other rows are empty, forming zig-zag chains running along $[10\bar{1}]_r$.

S2. SCRUTINYITE (α-PbO_2) STRUCTURE

The scrutinyite(*s*), or α-PbO_2, crystal structure of SnO_2 is orthorhombic, adopts the space group Pbcn (No. 60), and has lattice parameters $\mathbf{a}_s$ = 4.714 Å, $\mathbf{b}_s$ = 5.727, and $\mathbf{c}_s$ = 5.214 Å.[7] The fractional positions of the oxide ion (O^{2-}) are approximately (based on computations[8]) 0.277, 0.388, 0.418 and of the tetravalent tin (Sn^{4+}) are 0, 0.165, 0.25 (with computed lattice parameters of $\mathbf{a}_s$ = 4.707 Å, $\mathbf{b}_s$ = 5.710, and $\mathbf{c}_s$ = 5.246[8]). The relationship between the scrutinyite and rutile lattice parameters are as follows: $\mathbf{a}_s \approx \mathbf{a}_r$, $\mathbf{b}_s \approx \mathbf{2c}_r$, and $\mathbf{c}_s \approx \mathbf{b}_r$.

For simplicity of comparison between the structures, we use the non-standard Pcnb setting of space group No. 60 for *s*-SnO_2. In this setting, which is effectively a 90 ° rotation about **a**, the lattice parameters are $\mathbf{a}_{s^*}$ = 4.714 Å, $\mathbf{b}_{s^*}$ = 5.214, and $\mathbf{c}_{s^*}$ = 5.727 Å (where the * denotes the non-standard crystallographic setting) and $\mathbf{a}_{s^*} \approx \mathbf{a}_r$, $\mathbf{b}_{s^*} \approx \mathbf{b}_r$, and $\mathbf{c}_{s^*} \approx \mathbf{2c}_r$. (The fractional positions of the oxide ion O^{2-} are 0.277, 0.418, 0.388 and of the tetravalent tin Sn^{4+} are 0, 0.25, 0.165.) The comparable distances in rutile are : $\mathbf{a}_r$ = 4.738, $\mathbf{b}_r$ = 4.738, $\mathbf{2c}_r$ = 6.374 Å. Note that the $\mathbf{b}_{s^*}$ axis is significantly (10 %) larger than $\mathbf{b}_r$, and $\mathbf{c}_{s^*}$ is significantly (10 %) smaller than $\mathbf{2c}_r$.

Using the Pcnb setting, the $(100)_{s^*}$ and $(010)_{s^*}$ planes are structurally similar to the $(100)_r$ planes. These both can be considered eutactic planes and stacking along them is hexagonal close-packed (*hcp*), as in rutile. These planes are shown respectively in Figure S2(a) and (b). Cation stacking in the primary $(100)_{s^*}$ plane differs from that in rutile, with ½ of every *c* row running along $[001]_{s^*}$ being filled along the **c** axis, leading to zig-zag chains running along the $[010]_{s^*}$ in the $(100)_{s^*}$. This pattern we call $c_{½\text{-}II}$ (which is equivalent to the XY-II nomenclature by Morris[4, 5]).

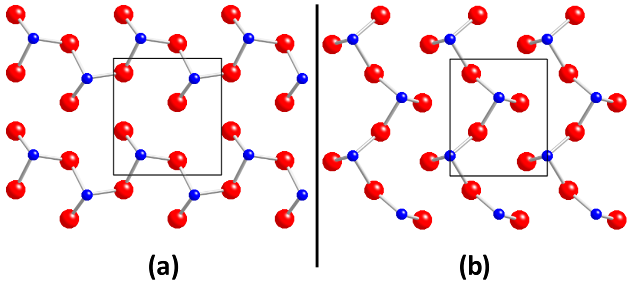

Figure S2. (a) The $(100)_{s^*}$ plane of scrutinyite (*s**) SnO_2. The **b** (**c**) axis is horizontal (vertical). (b) The $(010)_{s^*}$ plane of *s**-SnO_2. The **a** (**c**) axis is horizontal (vertical). Red (blue) spheres are O^{2-} anions (Sn^{4+} cations) and bonds are white cylinders.[6]

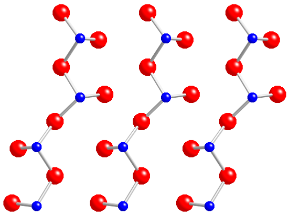

Figure S3. The $(012)_{s^*}$ plane of scrutinyite (*s**) SnO_2. The **a** axis is horizontal and the $[02\bar{1}]_{s^*}$ direction is vertical. Red (blue) spheres are O^{2-} anions (Sn^{4+} cations) and bonds are white cylinders.[6]

The change in cation packing pattern in the primary $(100)_{s^*}$ eutactic plane renders the $(010)_{s^*}$ plane inequivalent to it (unlike rutile) and leads to orthorhombic symmetry. The resultant cation packing for the for this (now secondary) eutactic $(010)_{s^*}$ plane is similar to the $\ldots Aa_{1/4}c_{1/4\text{-}I}Bb_{1/4}c_{1/4\text{-}I}\ldots$ observed for the $(101)_r$. Considering the bond connectivity of cations above an *A* plane, tin cations fill ½ of every other *c* and *a* sites in rows running along the $[001]_{s^*}$ (vertical in Figure S2(b)), while the other rows are empty, forming zig-zag chains running along $[001]_{s^*}$. The $(010)_{s^*}$ is more distorted than the $(100)_{s^*}$ in *s*-SnO$_2$. It is important to note the distinct similarity between the $(101)_r$ plane of rutile (Figure S1(b)) and the $(010)_{s^*}$ plane of scrutinyite (Figure S2(b)).

The $(012)_{s^*}$ and $(102)_{s^*}$ in Pcnb *s**-SnO$_2$ are the geometric equivalents to the $(101)_r$ of *r*-SnO$_2$ (according to the lattice parameter relationships). The $(012)_{s^*}$ is shown in Figure S3, as it retains the geometric similarity in the oxygen packing to the $(101)_r$. Again, we use eutactic packing terms to describe this plane. (The $(102)_{s^*}$ is so severely distorted that it no longer shares such atom stacking similarities, and is thus not shown). The cation stacking for the tertiary $(012)_{s^*}$ eutactic plane is different than the other planes, and we call it $a_{1/4}c_{1/4\text{-}II}$. Above an *A* anion plane, the tin cations fill ½ of every *a* and *c* row running along the $[02\bar{1}]_{s^*}$, as in $a_{1/4}c_{1/4\text{-}I}$, forming zig-zag chains that alternate every two tin cations in $a_{1/4}c_{1/4\text{-}II}$ stacking rather than every one in $a_{1/4}c_{1/4\text{-}I}$ stacking. Using these descriptions, of cation stacking in eutactic planes, allows one to describe cation packing errors (cation stacking faults) in otherwise *ABAB* eutactic packing of distorted hexagonal (or tetragonally packed) anion nets.

S3. COLUMBITE STRUCTURE

The columbite (*c*) structure is an ordered superstructure of the scrutinyite structure that forms for some materials of the stoichiometry B'B$_2$O$_6$.[9-11] The B' cation is ordered into every third $(100)_s$ cation plane of the scrutinyite structure, resulting in a tripled $\mathbf{a}_s$ axis and generation of two distinct cationic sites and three distinct oxide ion sites. The space group remains Pbcn. The relationship between the columbite and scrutinyite lattice parameters are as follows: $\mathbf{a}_c \approx \mathbf{3a}_s$, $\mathbf{b}_c \approx \mathbf{b}_s$, and $\mathbf{c}_c \approx \mathbf{c}_s$.

For simplicity of comparison to rutile, we also use the non-standard Pcnb setting for columbite (*c**), where $\mathbf{a}_{c^*} \approx 3\mathbf{a}_{s^*}$, $\mathbf{b}_{c^*} \approx \mathbf{b}_{s^*}$, and $\mathbf{c}_{c^*} \approx \mathbf{c}_{s^*}$. For *c**-CoNb$_2O_6$, $\mathbf{a}_{c^*} = 14.12$, $\mathbf{b}_{c^*} = 5.036$, and $\mathbf{c}_{c^*} = 5.701$.[12, 13] In this work, the tripled axis is not of major importance and, to facilitate direct comparisons to rutile and scrutinyite, we consider the following distances : $\frac{1}{3}\mathbf{a}_{c^*} = 4.707$, $\mathbf{b}_{c^*} = 5.036$, and $\mathbf{c}_{c^*} = 5.701$. (The local cation to cation distances along $\mathbf{a}_{c^*}$ are ≈ 4.55, 4.79, and 4.79 Å, illustrating that there are local deviations from the average). If we ignore the order between Co and Nb cations, the cation structure can be considered simply as that of scrutinyite. Hence, columbite should support the growth of scrutinyite from both geometric and bonding perspectives. In the rest of the document, we use the *c**-CoNb$_2$O$_6$ structure for indexation and the scutinyite approximation to determine misfit strains and epitaxial *ORs*.

S4. RELEVANT CRYSTALLOGRAPHIC PLANES

Epitaxial orientation relationships (*ORs*) are usually written by stating a pair of parallel planes between the film and substrate, normally with respect to the substrate's surface plane, along with a direction in each plane that are aligned with one another. In combinatorial substrate epitaxy (*CSE*),[14-16] using the substrate's surface plane is not practical since each polycrystal has a different surface. Instead, we consider the relationship between important structural planes, such as the eutactic planes described above, or low-energy planes that exist on the Wulff shape of the crystal, or low-index planes that bound orientation space.

The eutactic planes have already been described: for rutile they are $(100)_r$ and $(101)_r$. Some low-energy planes are, in order increasing energy for SnO$_2$:[17-19] $(110)_r$, $(100)_r$, $(101)_r$, $(201)_r$, and $(001)_r$. For TiO$_2$, the $(201)_r$ is not on the Wulff shape, while the $(001)_r$ is only a point on it.[20] The bounding planes in orientation space are $(100)_r$, $(001)_r$, and $(110)_r$.[21] As such, there are 5 planes of interest: $(110)_r$, $(100)_r$, $(101)_r$, $(201)_r$, and $(001)_r$.

If we were to use an orthorhombic cell for rutile that had the size of the cell for Pcnb scrutinyite (a doubled **c** axis), there would be 8 planes of interest based on the above descriptions: $(110)_{s^*}$, $(100)_{s^*}$, $(010)_{s^*}$,$(012)_{s^*}$, $(102)_{s^*}$, $(101)_{s^*}$, $(011)_{s^*}$, and $(001)_{s^*}$. This is useful because there is much less known about the scrutinyite polymorph than there is of rutile. Based on the little we know of scrutinyite SnO$_2$, described in the next paragraph, these 8 planes are the primary planes of interest.

The eutactic planes in scrutinyite (and its approximation for columbite) are $(100)_{s^*}$, $(010)_{s^*}$, and $(012)_{s^*}$. (Again, the $(102)_{s^*}$ is too distorted to be considered eutactic.) The energy of only four planes have been calculated for scrutinyite structured TiO$_2$ (or TiO$_2$-II);[22] in order increasing energy they are: $(100)_{s^*}$, $(010)_{s^*}$, $(101)_{s^*}$, and $(001)_{s^*}$. Similar expectations are likely in the SnO$_2$ system, but not all of the equivalent rutile planes have been considered in the literature for the scrutinyite structure. Finally, the bounding planes in orientation space are $(100)_{s^*}$, $(010)_{s^*}$, and $(110)_{s^*}$.[21]

S5. STANDARD STEREOGRAPHIC PROJECTIONS

The standard plotting of orientation data uses stereographic projections, and all of orientation space is condensed into the standard triangle needed to cover all unique orientations.[21] The standard stereographic triangles are shown in Figure S4 for tetragonal *r*-SnO$_2$ (left) and orthorhombic *s**-SnO$_2$ (right), with the approximate location of the planes described above marked thereon. The angular space along the straight edges of the triangle are 90 °. The angular space along the curved edges are 45 ° for rutile and 90 ° for scrutinyite (*s**). The angular distance between $(001)_r$ / $(102)_r$ and $(100)_r$ / $(101)_r$ for *r*-SnO$_2$ are 36.6 ° and 33.9 °, respectively (values were computed using CrystalMaker[6]). The angular distance between $(001)_{s^*}$ / $(102)_{s^*}$ and $(100)_{s^*}$ / $(101)_{s^*}$ for *s**-SnO$_2$ are 31.3 ° and 39.5 °, respectively, while the angular distance between $(001)_{s^*}$ / $(012)_{s^*}$ and $(010)_{s^*}$ / $(011)_{s^*}$ for *s**-SnO$_2$ are 28.8 ° and 42.3 °, respectively. Finally, the angular distance between the $(100)_{s^*}$ / $(110)_{s^*}$ for *s**-SnO$_2$ is 42.1 °. Keep in mind that the **c*** axis lattice parameter is doubled in the *s**-SnO$_2$ structure compared to the rutile structure, which results in similar planes having different indexations. Several such triangles have been presented in the main text. When the structures are described as above, the rutile triangle can be reflected across the $(001)_r$-$(110)_r$ edge to generate the larger triangle of scrutinyite (*s**). Thus, the similarities are easily described.

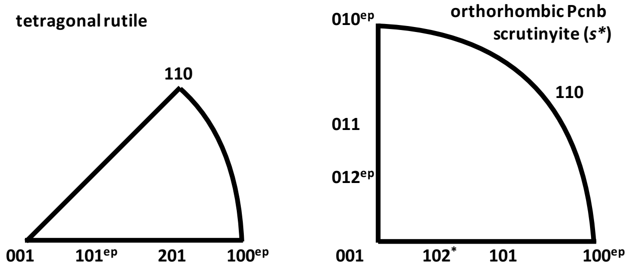

Figure S4. Standard stereographic triangles for rutile and scrutinyite (in the Pcnb setting) structured SnO_2. Important planes are overlaid on the diagrams, as discussed in the text.

S6. EPITAXIAL ORIENTATION RELATIONSHIPS (*ORs*)

Because most epitaxy is described using planar matching, owing to the preponderance of work done using low-index single crystals as substrates, it is helpful to describe the expected planar matching. In our work using polycrystalline substrates in *CSE*, we have found that usually one or two planar *ORs* are sufficient to describe epitaxy over all of orientations space. In general, we have found that, for eutactic crystal structures, the alignment of the eutactic planes and directions is a simple descriptor for the experimentally observed *ORs*.[14, 16, 23] As described in the main text, this remains true for growth of *r*-SnO_2 and *s*-SnO_2 on *c*-$CoNb_2O_6$ substrates. Thus, we consider the planar matches of all the pseudo-eutactic planes described previously (Figure S1, S2, and S3) for their expected epitaxial misfit strains. In other words, we focus on the strains arising from aligning $(100)_r$, $(101)_r$, $(100)_{s^*}$, $(010)_{s^*}$, and $(012)_{s^*}$. To complete the stereographic triangle, we include also the strains from alignment of the $(001)_r$ and $(001)_{s^*}$ (but do not include cation stacking for these non-eutactic planes). For simplicity sake, we use the Pcnb scrutinyite (*s**) unit cell for comparison. For the three structures, repeat periods along directions of interest are given in Table S1.

Table S1: Comparable repeat periods for materials[a,b]

	***r**-SnO_2**	***s**-SnO_2**	***c**-$CoNb_2O_6$**
<100>	**4.738**	**4.714**	**4.713**
<010>	**4.738**	**5.214**	**5.037**
<001>	**6.374[c]**	**5.727**	**5.701**
½<02$\bar{1}$>[d]	**5.710[d]**	**5.949**	**5.788**

[a] All structures are described using a Pcnb scrutinyite (*s**) unit cell.

[b] All units are in Å

[c] The $<001>_r$ is ½ of this value: 3.187 Å

[d] This is the $<10\bar{1}>_r$ length

We consider the epitaxial *ORs* for *s**-SnO_2 and *r*-SnO_2 on c*-$CoNb_2O_6$ (Table 1 and Table S2), which occur on initial nucleation, and for *r*-SnO_2 on *s**-SnO_2 (Table S2), which could occur during growth on relaxed *s**-SnO_2 films. In Tables 1 and S2, the type of cation stacking present for all eutactic *ORs* is given, as are the percentage misfit strains along specific orthogonal directions within the plane. Highlighted in light grey are the epitaxial interfaces that have identical cation stacking, which are expected to be of lower energy as they avoid interfacial energy penalties from near-neighbor bonding (no cation packing disorder), and epitaxial misfit strains below 4 %, which minimize volumetric strain energy.

Table S2: Cation stacking[a] and epitaxial strains[b,c] for the (nearly) eutaxial planes of *r*-SnO_2 on *s-SnO_2[d] and for the non-eutaxial {001} planes of *s**- and r-SnO_2 on *c**-$CoNb_2O_6$[e] and *s**-SnO_2.**

Substrate	***Film***		
		***r*-SnO_2**	
***s**-SnO_2**	$\{100\}_r$ $[010]_r/[001]_r$	$\{010\}_r$ $[100]_r/[001]_r$	$\{101\}_r$ $[010]_r/[10\bar{1}]_r$
$\{100\}_{s*}$ $[010]_{s*}/[001]_{s*}$	$c_{1/2-I}$ / $c_{1/2-II}$ +10.0 / -10.2	$c_{1/2-I}$ / $c_{1/2-II}$ +10.0 / -10.2	$a_{1/4}c_{1/4-I}$ / $c_{1/2-II}$ +10.0 / +0.3
$\{010\}_{s*}$ $[100]_{s*}/[001]_{s*}$	$c_{1/2-I}$ / $a_{1/4}c_{1/4-I}$ -0.5 / -10.2	$c_{1/2-I}$ / $a_{1/4}c_{1/4-I}$ -0.5 / -10.2	$a_{1/4}c_{1/4-I}$ / $a_{1/4}c_{1/4-I}$ -0.5 / +0.3
$\{012\}_{s*}$ $[100]_{s*}/[02\bar{1}]_{s*}$	$c_{1/2-I}$ / $a_{1/4}c_{1/4-II}$ -0.5 / -6.7	$c_{1/2-I}$ / $a_{1/4}c_{1/4-II}$ -0.5 / -6.7	$a_{1/4}c_{1/4-I}$ / $a_{1/4}c_{1/4-II}$ -0.5 / -4.2
		$\{001\}_{s*,r}$[f]	
	***s**-SnO_2**	$[100]_{s*,r}/[010]_{s*,r}$	***r*-SnO_2**
***c**-$CoNb_2O_6$**	**0.0 / -3.4**		**-0.5 / +6.3**
***s**-SnO_2**	**0.0 / 0.0**		**-0.5 / +10.0**

[a] Written as film / substrate pairs using notation in §S1-S3

[b] See Tables S1 for values

[c] All units are in % determined by: $(d_{subs} - d_{film}) / d_{film} * 100$

[d] scrutinyite (*s**) is described using a Pcnb unit cell.

[d] *c**-$CoNb_2O_6$ is described using a Pcnb scrutinyite (*s**) unit cell (no tripling).

[f] Since this is not a eutactic plane, cation packing is not listed

S7. RAW HIGH-RESOLUTION IPF AND IQ MAPS FROM THE *LGR* SAMPLE

The unprocessed high-resolution inverse pole figure(*IPF*) map of (a) the substrate and (b) the *lgr* (low growth rate) 20 nm thick SnO_2 film is given in Figure S5. The grain shapes and boundaries are easily identified in the raw images. Poorly indexed pixels show up as "randomly" (or rainbow) colored pixels in an otherwise uniform region of coloration. Large collections of rainbow pixels are from pores, grain pullout, or scratches on the substrate surface. The vast majority of pixels are associated with the well indexed points, though more poorly indexed pixels are observed in the film, which generally has lower quality *EBSD* patterns.

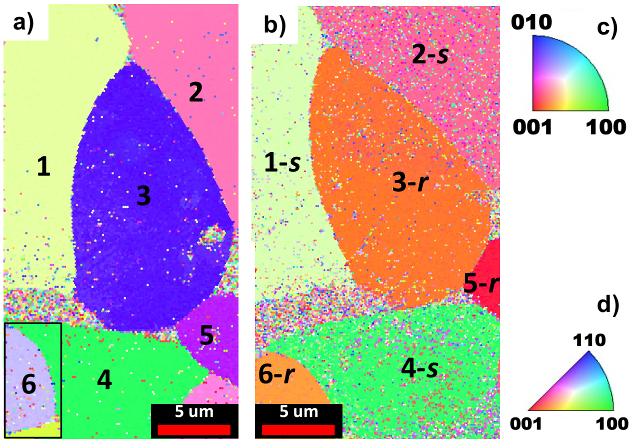

Figure S5. High resolution, small area, unprocessed *IPF* maps from (a) the substrate, indexed as *c**-$CoNb_2O_6$ (Pcnb setting), and (b) the overlaying film, indexed as the best match for both *s**-SnO_2 (Pcnb setting) and *r*-SnO_2. The color keys are given in (c) for the *c**-$CoNb_2O_6$ and *s**-SnO_2, and in (d) for the rutile *r*-SnO_2. 6 grains common to both are marked in (a) and (b), with the phase of each film grain also marked in (b). The area and aspect ratio of (a) is slightly different from (b), so the region between grain 6 and 4 are pasted as an inset in (a).

The image quality (*IQ*) is a metric that describes the relative sharpness of the *EBSD* pattern. Regions of different phase formation do not necessarily have worse image qualities, but regions of surface morphology, surface damage, overlapping local patterns, etc. do show up as lower *IQ*s. The *IQ* maps are given in Figure S6 for the substrate and film from the same region as shown in Figure S5. The majority of regions of low *IQ* is similar in the film and substrate, though more regions of low *IQ* exist in the film. The low *IQ* is almost always associated with the randomly colored pixels in the *IPF* maps, including those in film grains above well-indexed substrate grains.

With respect to understanding growth and phase stability, these poorly indexed, low *IQ* points can be ignored. Processing the data using grain dilation and orientation averaging provides an average description of what occurs on each crystal (grain) surface, similar to standard X-ray diffractograms on single crystals, which integrate over the entire area. Regions of low-*IQ* and unindexable points in an X-ray pattern would not be identifiable. Processing the data in Figure S5 result in the maps in Figure 1, which allow for straightforward discussion of competitive polymorph growth.

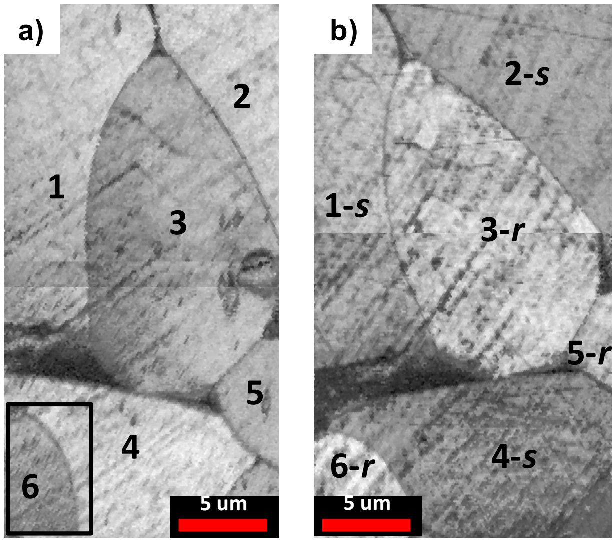

Figure S6. High resolution, small area, image quality (*IQ*) maps from (a) the substrate and (b) the overlaying film. Some grains common to both are marked in (a) and (b), with the phase of each film grain also marked in (b). The area and aspect ratio of (a) is slightly different from (b), so the region between grain 6 and 4 are pasted as an inset in (a).

S8. PARAMETERS FOR SIMULATION AND DICTIONARY INDEXING OF EBSD PATTERNS

Because of the similarity between the structures, especially along the eutactic directions described above, we carried out simulations of *EBSD* patterns to ensure one could truly differentiate them and confirm the commercial software index assignments. In the main text, we compare several experimental and simulated patterns (see Figure 2). Those patterns were generated using the methods described elsewhere using the values given below.[24-26] The meaning of all terms is described in the prior work. Additionally, we used a dictionary indexing approach on a small region of the slowest grown sample, to compare a given experimental pattern to simulated patterns of both relevant phases. The best fit pattern for both phases were determined and stored. Usually, a fit could be found for both phases, but one phase was always a significantly better fit than the other. These results confirmed the commercial indexations used elsewhere in the main text.

Monte Carlo simulations of all back scattered electrons were carried out for both phases using 70 ° incident 20 keV electrons, with a maximum escape depth of 100 nm (binned at 1 nm), considering returning electrons between 10 and 20 keV (binned at 1 keV). These electron simulations were used to generate a master pattern of 1001x1001 pixels with a minimum considered inter-planar *d*-spacing of 0.05 nm. From the master pattern, a dictionary of experimental patterns was generated in a dynamic fashion using the following parameters: -8.0° tilt angle for the camera, 23732.83 µm distance between the scintillator and illumination point, 133.34 µm wide pixels in a 244 x 244 pixel array on the scintillator, a pattern center at 0.63/76.90 pixels in x/y, 150 nA beam current with a 100 µs dwell time, and a gamma corrected intensity using a factor of 0.3, along with exact energy averaging. The dictionary indexing method collected the top 50 matches between the experimental and dictionary images, the latter generated from a uniform sampling of the cubochoric orientation representation using 100 sampling points along the cubic semi-edge,[24] and used the top 20 to determine the orientation similarities and average best orientation.

S9. RAW LARGE AREA IPF MAPS FROM THE *LGR* SAMPLE

The unprocessed low-resolution *IPF* map of (a) the substrate and (b) the *lgr* (low growth rate) 20 nm thick film is given in Figure S7. The grain shapes and boundaries are easily identifiable, but less well defined in these raw images as compared to the high-resolution image in Figure S5. The area and aspect ratio of each is slightly different from the other and to match grains see the main text. Poorly indexed pixels show up as “randomly” (or rainbow) colored pixels in an otherwise uniform region of coloration. Large collections of rainbow pixels are from pores, grain pullout, or scratches on the substrate surface.

For the substrate, a majority of pixels are associated with well indexed points, and collections of poorly indexed points are generally associated with grain pullout. For the film, there are considerably more regions of poorly indexed points, because the film generally has worse *EBSD* patterns. When using the standard processing methods, the cleaned pattern results in Figure 3. As observed in Figure 3, there are significant regions over which an indexable film was not obtained. However, for many individual grains, quality film patterns were obtained. This is the power of *CSE* in investigating film growth: by using an ensemble of thousands of substrate grains simultaneously, a large number of successful growth observations can be found and used to generate a statistical understanding of epitaxial growth.

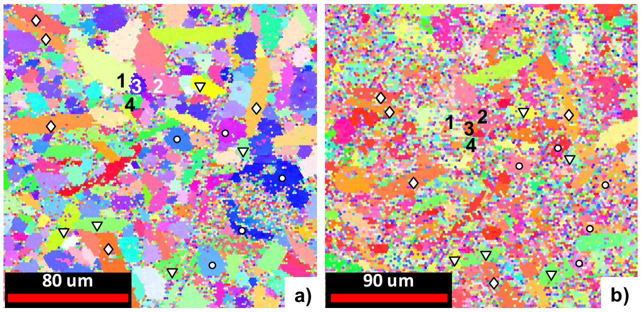

Figure S7. Large area unprocessed *IPF* maps from (a) the substrate, indexed as *c**-$CoNb_2O_6$ (Pcnb setting), and (b) the overlaying film, indexed as the best match for both *s**-SnO_2 (Pcnb setting) and *r*-SnO_2. Color keys for *IPF*s are identical to other figures. The area and aspect ratio of each is slightly different from the other.

S10. LARGE AREA IPF MAPS FROM THE *HGR* SAMPLE

Figures S8(a) and (b) are low resolution (0.6 μm), large area, processed *IPF* maps of (a) a region of a *c*-$CoNb_2O_6$ substrate and (b) the *hgr* 100 nm thick SnO_2 film grown upon it. In Figure S8(b), film grains were indexed using both *s*-SnO_2 (Pbcn setting) and *r*-SnO_2 structures. Note that the columbite and *s*-SnO_2 were indexed using the Pbcn setting, which is different from the main text. This is essentially a 90° rotation about **a**, and the transformation turns red grains in the main text Pcnb setting to be blue in this Pbcn setting. Figure S8(c) and (d) present the film *IPF* maps broken into (c) the *s*-SnO_2 grains and (d) the *r*-SnO_2 grains. The *s*-SnO_2 grains are colored greenish and blue, which correspond to the greenish to red observations in the main text for the *lgr* films indexed in Pcnb. The *r*-SnO_2 grains are red-toned. As discussed in the main text, there are relatively fewer (more) *s*-SnO_2 (*r*-SnO_2) grains observed in the *hgr* sample than in the *lgr* sample, but otherwise the observations are similar.

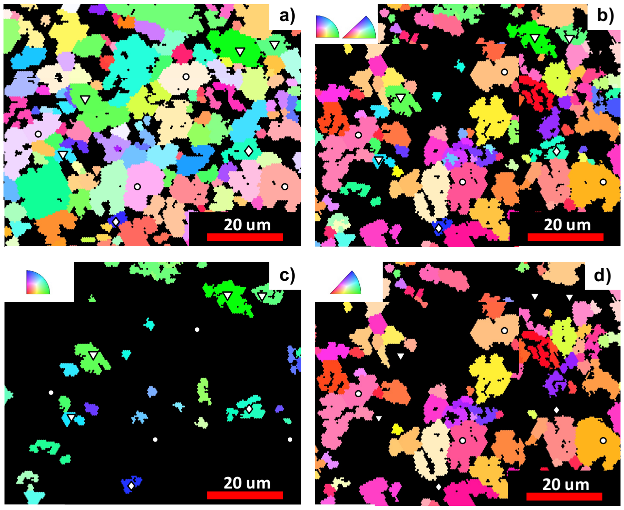

Figure S8. Large area *IPF* maps from (a) a substrate, indexed as *c*-$CoNb_2O_6$ (note: Pbcn setting), and (b) the overlaying *hgr* 100 nm thick film, indexed as the best match for both *s*-SnO_2 (note: Pbcn setting) and *r*-SnO_2. The same information as (b) is shown (c) and (d), with *s*-SnO_2 indexations in (c) and *r*-SnO_2 indexations in (d). Color keys for *IPF*s are shown as insets. Some locations in each are marked with different symbols.

S11. EPITAXIAL *ORs* EPITAXIAL IN THE *HGR* SAMPLE

56 total substrate-film grain pairs were identified from various regions of the *hgr* film, with 24 (32) film grains indexed as *s*-SnO_2 (*r*-SnO_2). In Figure S9(a) for the 24 *s*-SnO_2 grains, we plot the angles between the normal to the primary eutactic planes (out-of-plane), and inset is the angle between similar directions in the eutactic planes (in-plane). All *s*-SnO_2 grains are aligned similarly with the substrate, adopting the primary eutaxial *OR* described in the main text. In Figure S9(b) for the 32 *r*-SnO_2 grains, we plot the angles between the normal to a secondary set (see §S1-S3) of eutactic planes (out-of-plane), and inset is the angle between similar directions in the secondary eutactic planes (in-plane). All of these *r*-SnO_2 grains are aligned similarly with the substrate adopting a secondary eutaxial *OR* described in the main text. The *s*-SnO_2 (*r*-SnO_2) grains have an average misorientation of 2.0 ° and 2.6 ° (2.7 ° and 2.9 °) for the out-of-plane and in-plane directions, respectively. The spread in angular orientation is likely due to specific relaxations of interfacial mismatches for different orientations.

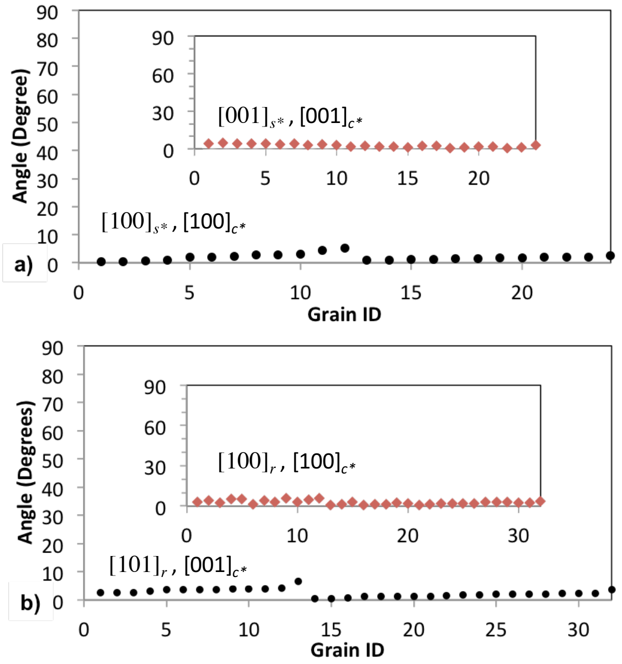

Figure S9. For the *hgr* 100 nm thick film, plots of the angle between: (a) the normals to the $(100)_{s*/c*}$ eutactic planes, i.e. $[100]_{s*/c*}$, and (inset) the in-plane $[001]_{s*/c*}$ directions for the *s*-SnO_2 grains and *c*-$CoNb_2O_6$ substrates; (b) the normals to the pseudo-eutactic planes $\{101\}_r$ and $(010)_{c*}$, i.e, ≈ $<102>_r$ and $[010]_{c*}$, and (inset) the in-plane $<010>_r$ and $[100]_{c*}$ directions for the *r*-SnO_2 grains and *c*-$CoNb_2O_6$ substrates.

S12. IPF MAPS FROM GRAINS USED IN TEM

Low resolution unprocessed *IPF* maps from regions of the (a) the *hgr* 100 nm thick film and (b) the *lgr* 20 nm thick film are shown in Figure S10. The marked green grains are those from which the *TEM* specimens were made, using a FIB liftout process and orienting the samples using *EBSD* to be along (001) zone axes.

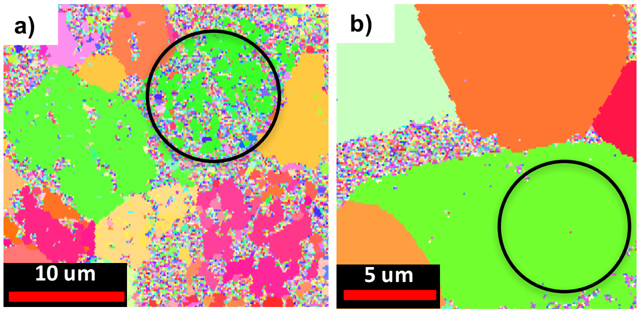

Figure S10. Low resolution unprocessed *IPF* maps from regions of the (a) the *hgr* 100 nm thick film and (b) the *lgr* 20 nm thick film, indexed as the best match for both *s*-SnO_2 (note these are indexed in the standard Pbcn setting) and *r*-SnO_2. Two grains marked are those from which the *TEM* specimens were made (in (b) this is grain 4 from Figures 1 and 3 in the main text).

S13. TEM FROM AN (001) GRAIN OF THE *LGR* SAMPLE

A low resolution bright field *TEM* image of the *lgr* film-substrate interface region is shown in Figure S11(a). The substrate is on the bottom while a bright region of damage to the 20 nm film is on the top. The film substrate interface is not easy to identify in this thin sample with surface damage. A high-resolution image from the interfacial region is shown in Figure S11(b). The substrate is on the bottom and the film on the top, with the interface between them**.** The interface normal is not in the plane of the image (i.e., perpendicular to the zone axis), and this leads to the interface spreading in the high-resolution *TEM* image. Throughout the image there is good atom registry, even though the interface is not clear. Figure S11(c) and (d) give the fast Fourier transform of the image for the film region (c) and substrate region (d). The substrate patterns have a tripling along [100], as expected for *c*-$CoNb_2O_6$. The spots from the **a** axis tripling are absent or faint in the film patterns: they should be absent in *s*-SnO_2, but the unavoidable overlap with the substrate in the titled interface results in some faint spots at these locations. These observations are provided as support that the two films are similar, but no firmer conclusions are derived from them.

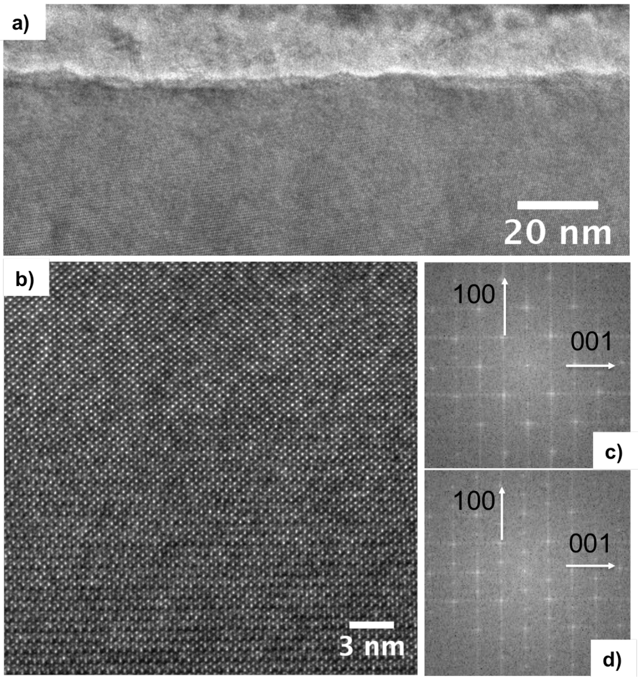

Figure S11. (a) A low-resolution *TEM* image of the *lgr* 20 nm thick film. (b) a high-resolution *TEM* image of the interfacial region: the substrate is on the bottom and film is on the top, with the interface between them, and difficult to distinguish. Fast Fourier transforms of (c) the film and (d) the substrate.

AUTHOR INFORMATION

Corresponding Author

* Paul A. Salvador, Department of Materials Science and Engineering, Carnegie Mellon University, 5000 Forbes Ave, Pittsburgh, PA 15213, paulsalvador@cmu.edu .

Present Addresses

§ Boopathy Kombaiah, Oak Ridge National Laboratory, P.O. Box 2008, Oak Ridge, TN 37831-6138, USA

Author Contributions

The manuscript was written through contributions of all authors. All authors have given approval to the final version of the manuscript.

Funding Sources

National Science Foundation grant DMR 1609355, CMU Grant MCF-677785, Air Force Office of Scientific Research (AFOSR): MURI program, contract # FA9550-12-1-0458.

Notes

The authors declare no competing financial interest.

ACKNOWLEDGMENT

JW, PAS, and GSR acknowledge the support of the National Science Foundation: grant DMR 1609355. FR and MDG acknowledge the support of the Air Force Office of Scientific Research (AFOSR): MURI program, contract # FA9550-12-1-0458. The authors acknowledge use of the Materials Characterization Facility at Carnegie Mellon University, supported by grant MCF-677785.

ABBREVIATIONS

c, columbite-structured; c*, columbite-structured in an *s** subcell; *CSE*, combinatorial substrate epitaxy; *EBSD*, electron backscatter diffraction; *FIB*, focused ion beam; *hcp*, hexagonal close-packed; *hgr*, high growth rate; *IPF*, inverse pole figure; *IQ*, image quality; *lgr*, low growth rate; *OR*, orientation relationship; *r-*, rutile-structured; *s*, scrutinyite structured; *s**, scrutinyite in Pcnb setting; *SAED*, selected-area electron diffraction; *SEM*, scanning electron microscopy; SI, supporting information; *TEM*, transmission electron microscopy; *TLK*, terrace-ledge-kink.

REFERENCES

(1) Bolzan, A. A.; Fong, C.; Kennedy, B. J.; Howard, C. J., Structural studies of rutile-type metal dioxides. *Acta Crystallographica Section B-Structural Science* **1997**, 53, 373-380.

(2) Rohrer, G. S., *Structure and Bonding in Crystalline Materials.* Cambridge University Press: 2004; p 540.

(3) West, A. R.; Bruce, P. G., Tetragonal-packed crystal structures. *Acta Crystallographica Section B* **1982**, 38, 1891-1896.

(4) J. W. Morris, J. Appendix: The Crystals Structures of Compounds. http://www.mse.berkeley.edu/groups/morris/MSE200/chap3a.pdf (2016).

(5) J. W. Morris, J. Lecture 20 Slides. http://www.mse.berkeley.edu/groups/morris/MSE200/Lecture_Notes/lecture slides-5.pdf (2016).

(6) *Images generated and distances/angles calcuated using CrystalMaker® (v. 9.2.6): a crystal and molecular structures program for Mac and Windows.* , CrystalMaker Software Ltd.: Oxford, England, 2016.

(7) Suito, K.; Kawai, N.; Masuda, Y., High-Pressure Synthesis of Orthorhombic SnO_2. *Materials Research Bulletin* **1975**, 10, 677-680.

(8) Gracia, L.; Beltran, A.; Andres, J., Characterization of the high-pressure structures and phase transformations in SnO_2. A density functional theory study. *Journal of Physical Chemistry B* **2007**, 111, 6479-6485.

(9) Pullar, R. C., The Synthesis, Properties, and Applications of Columbite Niobates ($M^{2+}Nb_2O_6$): A Critical Review. *Journal of the American Ceramic Society* **2009**, 92, 563-577.

(10) Sturdivant, J. H., The crystal structure of columbite. *Zeitschrift Fur Kristallographie* **1930**, 75, 88-108.

(11) de Dompablo, M. E. A. Y.; Lee, Y. L.; Morgan, D., First Principles Investigation of Oxygen Vacancies in Columbite MNb_2O_6 (M = Mn, Fe, Co, Ni, Cu). *Chemistry of Materials* **2010**, 22, 906-913.

(12) Husson, E.; Repelin, Y.; Dao, N. Q.; Brusset, H., Characterization of Different Bondings in Some Divalent Metal Niobates of Columbite Structure. *Materials Research Bulletin* **1977**, 12, 1199-1206.

(13) $CoNb_2O_6$ (Nb_2CoO_6 orth) Crystal Structure: http://materials.springer.com/isp/crystallographic/docs/sd_0378256. In *PAULING FILE: Inorganic Solid Phases, SpringerMaterials (online database)*, Villars, P., Ed. Springer-Verlag GmbH: 2016.

(14) Schultz, A. M.; Zhu, Y.; Bojarski, S. A.; Rohrer, G. S.; Salvador, P. A., Eutaxial growth of hematite Fe_2O_3 films on perovskite $SrTiO_3$ polycrystalline substrates. *Thin Solid Films* **2013**, 548, 220-224.

(15) Havelia, S.; Wang, S.; Balasubramaniam, K. R.; Schultz, A. M.; Rohrer, G. S.; Salvador, P. A., Combinatorial substrate epitaxy: a new approach to growth of complex metastable compounds. *CrystEngComm* **2013**, 15, 5434-5441.

(16) Zhang, Y.; Schultz, A. M.; Li, L.; Chien, H.; Salvador, P. A.; Rohrer, G. S., Combinatorial Substrate Epitaxy: A high throughput method for determining phase and orientation relationships and its application to $BiFeO_3/TiO_2$ heterostructures. *Acta Materialia* **2012**, 60, 6486-6493.

(17) Beltran, A.; Andres, J.; Longo, E.; Leite, E. R., Thermodynamic argument about SnO_2 nanoribbon growth. *Applied Physics Letters* **2003**, 83, 635-637.

(18) Xu, C. H.; Jiang, Y.; Yi, D. Q.; Sun, S. P.; Yu, Z. M., Environment-dependent surface structures and stabilities of SnO_2 from the first principles. *Journal of Applied Physics* **2012**, 111, 063504.

(19) Das, S.; Jayaraman, V., SnO_2: A comprehensive review on structures and gas sensors. *Progress in Materials Science* **2014**, 66, 112-255.

(20) Barnard, A. S.; Zapol, P., Effects of particle morphology and surface hydrogenation on the phase stability of TiO_2. *Physical Review B* **2004**, 70, 235403.

(21) Nolze, G.; Hielscher, R., Orientations - perfectly colored. *Journal of Applied Crystallography* **2016**, 49, 1786-1802.

(22) De Angelis, F.; Di Valentin, C.; Fantacci, S.; Vittadini, A.; Selloni, A., Theoretical Studies on Anatase and Less Common TiO_2 Phases: Bulk, Surfaces, and Nanomaterials. *Chemical Reviews* **2014**, 114, 9708-9753.

(23) Xu, Z.; Salvador, P. A.; Kitchin, J. R., First-Principles Investigation of the Epitaxial Stabilization of Oxide Polymorphs: TiO_2 on $(Sr/Ba)TiO_3$. *ACS Applied Materials & Interfaces* **2016**, 9, 4106–4118.

(24) Singh, S.; Graef, M. D., Orientation sampling for dictionary-based diffraction pattern indexing methods. *Modelling and Simulation in Materials Science and Engineering* **2016**, 24, 085013.

(25) Chen, Y. H.; Park, S. U.; Wei, D.; Newstadt, G.; Jackson, M. A.; Simmons, J. P.; De Graef, M.; Hero, A. O., A Dictionary Approach to Electron Backscatter Diffraction Indexing. *Microscopy and Microanalysis* **2015**, 21, 739-752.

(26) Callahan, P. G.; De Graef, M., Dynamical Electron Backscatter Diffraction Patterns. Part I: Pattern Simulations. *Microscopy and Microanalysis* **2013**, 19, 1255-1265.